2015-05-01

An Investigation of Off-Design Operation in High Suction Performance Inducers

Ryan Collins Cluff
Brigham Young University - Provo

An Investigation of Off-Design Operation in High Suction Performance Inducers

Ryan Collins Cluff

A thesis submitted to the faculty of
Brigham Young University
in partial fulfillment of the requirements for the degree of

Master of Science

Steven E. Gorrell, Chair
R. Daniel Maynes
W. Jerry Bowman

Department of Mechanical Engineering

Brigham Young University

June 2015

ABSTRACT

An Investigation of Off-Design Operation in High Suction Performance Inducers

Ryan Collins Cluff
Department of Mechanical Engineering, BYU
Master of Science

Three-dimensional two-phase unsteady CFD simulations were run on three and four-blade inducers for the purpose of analyzing differences in cavitation stability at design and off-design flow rates. At design flow rates, there were very small differences between the breakdown curves for the three and four-bladed inducers. However, at lower cavitation numbers, the three-bladed inducer exhibited up to three times the rotor forces than the four-bladed inducer. When moving to off-design flow rates, both inducers experienced multiple modes of cavitation instabilities including rotating cavitation, alternate-blade cavitation, and cavitation surge. The four-bladed inducer began experiencing the formation of these modes of instability beginning at a cavitation number of $\sigma = 0.047$ whereas the three-bladed inducer began at a cavitation number of $\sigma = 0.091$. Additionally, the three-bladed inducer showed rotor forces up to ten times higher than the four-bladed inducer at similar cavitation numbers.

Three-dimensional single-phase steady CFD simulations were run on four-blade inducer geometries with 7°, 9°, 11° and 14° inlet tip blade angles with a stability control device (SCD) installed. The simulations were ran at multiple flow coefficients. Results show interesting flow effects from the SCD. For example, at lower flow coefficients, the incidence angle actually decreases at greater than 70% span. This is due to a region of accelerated axial flow coming from the recirculation of the SCD which occurs near the shroud. Results also show strong correlations between efficiency and head rise to the local mass flow gain experienced due to the recirculating flow through the SCD. A best fit curve was generated to predict mass flow gain based on the inducer's inlet tip blade angle and flow coefficient. Based on this research, the ability to predict mass flow gain and consequently efficiency and head rise for similarly designed inducers with varying inlet blade angles has been demonstrated.

Keywords: axial inducer, turbopump, cavitation

ACKNOWLEDGMENTS

I would like to thank Dr. Gorrell and committee members for their constant support and guidance, the Fulton Supercomputing Lab for providing the tremendous resources needed for the simulations, CD-adapco for their technical support and training in using their CFD package, and NASA, through ConceptsNREC, for their financial support with the research for this thesis. And of course my family, whose confidence and love were driving forces to help me get to this point.

TABLE OF CONTENTS

LIST OF TABLES

LIST OF FIGURES

$$\phi = \frac{Q}{AU_{tip}}$$
$$\sigma = \frac{P_{01} - P_v}{\frac{1}{2}\rho U_{tip}^2}$$
$$\psi = \frac{P_{08} - P_{00}}{\rho U_{tip}^2}$$
$$\eta = \frac{\dot{m}_{00} * \frac{P_{02} - P_{00}}{\rho}}{T * \Omega}$$
$$NPSH = \left(\frac{P_1}{\rho g} + \frac{V_1^2}{2g}\right) - \frac{\rho_v}{\rho g}$$
$$NSS = \frac{N\sqrt{Q}}{NPSH^{0.75}}$$
$$CorrectedNSS = \frac{NSS}{(1 - (\frac{r_{1h}}{r_{1t}})^2)^{0.5}}$$
$$\alpha = \beta_b - \beta_1$$
$$S = \frac{c}{h}$$

α	Incidence Angle $[deg]$
β_1	Relative Velocity Flow Angle $[deg]$
β_b	Inlet Blade Angle $[deg]$
η	Efficiency $[-]$
μ	Dynamic Viscosity $[m^2/s]$
ρ	Density $[kg/m^3]$
σ	Cavitation Number $[-]$
ϕ	Flow Coefficient $[-]$
ψ	Head Rise Coefficient $[-]$
Ω	Rotational Speed $[rad/s]$
A	Inlet Area $[m^2]$
c	Blade Chord Length $[m]$
g	Gravity $[m/s^2]$
h	Blade Spacing $[m]$
K	Cavitation Compliance $[-]$
M	Mass Flow Gain Factor $[-]$
$\dot{m}$	Mass Flow Rate $[kg/s]$
N	Rotational Speed of Pump$[Rpm]$
$NPSH$	Net Positive Suction Head $[m]$
Nss	Net Suction Specific Speed $[-]$
P	Local Static Pressure $[Pa]$
Q	Volumetric Flow Rate $[m^3/s]$
S	Solidity $[-]$

T	Torque $[n-m]$
U_{tip}	Blade Tip Speed $[m/s]$
V	Local Fluid Velocity $[m/s]$
$\forbidden{V}$	Volume $[m^3]$

Subscripts, superscripts, and other indicators

$[\,]_0$	indicates [ ] is a property at the inlet of the domain
$[\,]_{0(\,)}$	indicates [ ] is a stagnation property according to the ( ) subscript
$[\,]_1$	indicates [ ] is a property at 2mm upstream of leading edge of inducer
$[\,]_2$	indicates [ ] is a property at 2mm downstream of trailing edge of inducer
$[\,]_8$	indicates [ ] is a property at the outlet of the computational domain
$[\,]_C$	indicates [ ] is of the vapor cavity
$[\,]_{norm}$	indicates [ ] is normalized by the I7no inducer at 100% flow
$[\,]_h$	indicates [ ] is a property at the hub of the rotor blade
$[\,]_t$	indicates [ ] is a property at the tip of the rotor blade
$[\,]_v$	indicates [ ] is a property of the vapor state

CHAPTER 1. INTRODUCTION

1.1 Background

The use of inducers is often required for any application where fluid is drawn with very low inlet pressures (high suction specific speed or NSS). There exist many industries where it is advantageous to be able to operate at as low of inlet pressures as possible. For example, liquefied natural gas transfer pumps transfer natural gas from one holding tank to another. The ability to operate at high NSS results in transferring more fuel in a single run. Another common application is in space launch vehicles. Developing a pump with higher NSS allows for a reduced propellant tank pressure. A reduced tank pressure reduces the structural requirements for the tank which results in a lighter vehicle and reduced overall payload cost. Other common applications include aircraft fuel pumps and boiler feed pumps.

A typical pump that incorporates an inducer is configured in at least two stages: the first stage consists of an inlet pump impeller or inducer, and the second stage is a high-head-rise centrifugal impeller. Figure 1.1 shows a standard pump configuration with an inlet inducer followed by an integral centrifugal impeller.

The role of the inducer is to raise the propellant's pressure to a level adequate to allow the downstream components (typically the centrifugal impeller stage) to operate without the presence of cavitation. Cavitation refers to when a fluid's local pressure drops below its vapor pressure and vapor cavities form, normally along the suction side of the blade. Generally, designers are less concerned about the inception of cavitation, as this is not a particularly severe process. However, as the zone of cavitation grows, it can begin to block the fluid from moving through the pump. When this happens, the pump is no longer able to accomplish its task of delivering flow at the desired head and several debilitating effects occur such as:

1. large reduction in head rise (also known as breakdown) when the vapor cavity reaches the size of the inducer's inlet throat

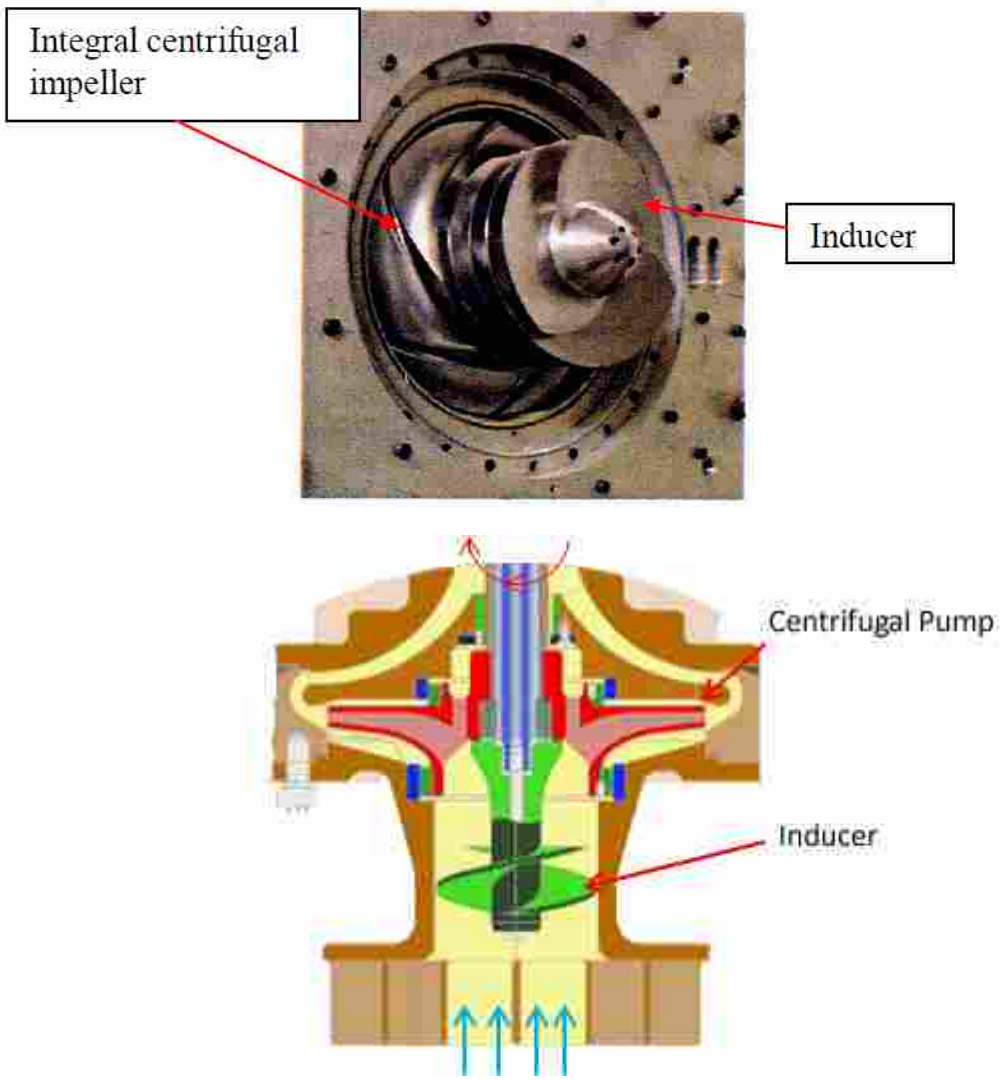

(b) Image taken from *July 2004 Newsletter*, Lawrence Pumps Inc; http://www.lawrencepumps.com/Newsletter/news_v01_i2_july.html

Figure 1.1: Image and cross-section diagram of a standard rocket turbopump inducer with integral centrifugal downstream impeller.

2. blade damage caused by the growth and collapse of cavitation bubbles

3. blade structural failure and inconsistent mass flow rates. This can cause catastrophic changes in engine thrust and is generated by large instabilities due to the interaction between the flow and the vapor cavities.

Significant research has been performed to develop standard design criteria for inducers. The theoretical optimum suction performance at a given flow coefficient is known as the Brumfield criterion [5] [6]. Figure 1.2 shows Brumfield's criteria along with several cold water inducer

tests [1]. As flow coefficient decreases, Corrected NSS grows exponentially. Corrected NSS takes into account the ratio of the hub to tip radius. In other words, high NSS can be achieved by designing an inducer that operates at low flow coefficients. One challenge that arises at low flow coefficients is maintaining the proper level of flow incidence (flow angle relative to the inducer blade). It has been shown that ideally, an inducer should maintain a nominal incidence angle of $+2^\circ$ [2]. In order to keep a $+2^\circ$ incidence angle at lower flow coefficients, inducers require smaller inlet blade angles. Smaller inlet blade angles have the negative effect of blocking the throat area and can lead to premature breakdown. Additionally, such an inducer has difficulty operating at off-design flow rates [5]. This is mostly because at low flow-coefficients, a small change in flow rate results in a large change in incidence angle, and large incidence angles contribute to the formation of cavitation. Recent research has begun investigating new techniques to eliminate these limitations of operating at low flow coefficients.

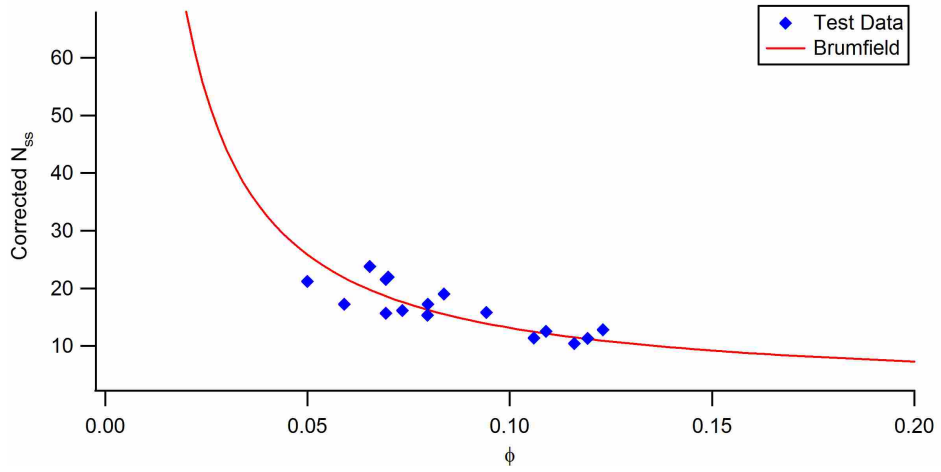

Figure 1.2: Corrected N_{ss} as a function of flow coefficient for various cold water inducer tests compared to Brumfield criterion [1]

Previous research by Krise [3] has shown that the use of a stability control device (SCD) may help to reduce the instabilities that are generated at the leading edge of the inducer. The SCD has a recirculation path that diffuses the unstable fluid near the tip of the inducer and reintroduces it upstream. The inlet of the SCD is located at a mid-point within the blade region of the inducer, and the outlet of the SCD is located upstream of the blade leading edge. This recirculation essentially creates a local mass flow increase within the inducer region and effectively decreases the

incidence which has a stabilizing effect to the flow. Figure 1.3 shows a diagram of the SCD and the recirculating flow.

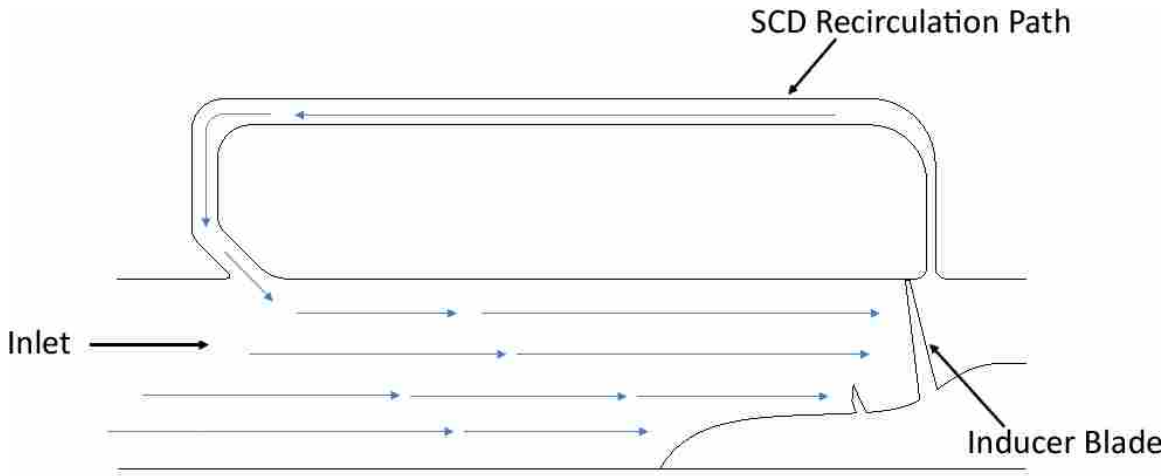

Figure 1.3: Diagram of Stability Control Device (SCD).

1.2 Objectives

Significant work has been made in assisting in the design process for a standard inducer. Given certain requirements such as net specific suction head (NPSH), range of operating flow coefficients, and blade angle, it is a fairly straightforward process to create an inducer design as well as have reasonable expectations of performance and stability. Designing for an inducer with a SCD is not as straight forward. Preliminary work performed by Krise [3] laid the groundwork for this research. It was shown that with a SCD, cavitation inception was delayed. It also showed an overall stabilizing effect to the flow, especially when operating at off-design flow rates. It is the goal of this research to continue building a knowledge base for inducers with a SCD. This will be done by analyzing how certain flow characteristics, such as incidence angle and head rise, change once a SCD is introduced. Additionally, work will be made to develop methods for predicting major pump performance metrics (such as head rise, incidence, and efficiency) for inducers that use a SCD, based on pump design.

1.3 Thesis Organization

This thesis begins with chapter 2 which gives a review of current literature that discusses work done in the context of delaying and controlling cavitation instabilities in high speed inducers. A detailed description of methods employed for this research is given in chapter 3. This research employs computation fluid dynamics (CFD) to assist in the design and analysis in this work. In chapter 4, cavitation instabilities are investigated for three-bladed and four-bladed inducers without a SCD. There does not exist much research comparing the two inducer designs, and knowing the proper number of blades will be needed for the second half of this research. In chapter 5, a series of steady single-phase CFD simulations with a variety of inducer geometries are performed. The simulations vary flow rates, inducer inlet blade angle, and blade solidity. Based on the results of these simulations, an analysis is performed to attempt to predict pump characteristics such as head rise, efficiency, and incidence. Finally, the thesis concludes with chapter 6 to summarize the work performed and contributions made. Chapter 4 is a manuscript presented at the 49th American Institute of Aeronautics and Astronautics Joint Propulsion Conference. Chapter 5 is a manuscript in development for submission as a journal article. The formatting of the papers have been modified to meet the stylistic requirements of this thesis.

CHAPTER 2. LITERATURE REVIEW

2.1 Overview of Inducers

In applications where the pump's ability to operate with low inlet pressure conditions is important, inducers are often used. An inducer is an additional pump stage located at the axial inlet portion of the turbopump [4]. There are some inducers that are integral with the centrifugal pump, and others that are attached to the shaft further upstream of the centrifugal pump.

A pump's suction performance can be measured by its ability to operate at low inlet pressures. It is generally the goal of an inducer to achieve high suction performance, however, higher suction performance is often accompanied by weaker structural integrity. For example, Japiske et. al. [5] talks about a common design criteria equation (equation 2.1) that relates net suction specific speed (N_{ss}) with the inlet blade tip radius (r_{t1}), the inlet hub radius (r_{h1}), and the blade cavitation coefficient (σ_b).

$$N_{ss}^2 / \left(1 - \frac{r_{h1}^2}{r_{t1}^2}\right) = 3.420 / \left(\sigma_b (1+\sigma_b)^{0.5}\right) \tag{2.1}$$

According to equation 2.1, in order to attain high levels of suction performance, the blade tip radius must increase. A larger tip radius will create blade stresses that are higher and can lead to failure. Designing with structural integrity in mind requires providing for blade and hub stresses due to blade loading, flow instabilities, and centrifugal forces. It also requires proper choice of material that is both compatible with test and operating fluids. [4]

There exists a large variety of inducer types. Some have a cylindrical hub and shroud where their diameters are constant throughout, others have a tapered hub and shroud where the diameters change as you move upstream to downstream. There's a lot of variety in number of blades as well. Inducers commonly have anywhere between 2 and 6 blades. There even exist hubless inducer designs where the blades are supported and driven by the rear portion of the inducer blading or by

the shroud itself; however, any benefits that would come with a hubless inducer design are washed out because of the manufacturing costs and difficulties. [4]

2.2 Overview of Cavitation

Cavitation begins when a pure liquid is subjected to a pressure below its vapor pressure. When this happens, the fluid is said to be under tension. It will remain in this state of tension until either the pressure returns to a level above the vapor pressure or a nucleation site is introduced to enable the fluid to change to a vapor. Nucleation sites often come in the form of micro bubbles found in impurities within the fluid, along fluid boundaries with a solid surface, and even small temporary gaps between molecules due to thermal motion of the molecules [7]. Once the cavitation bubble forms, it is often convected to higher-pressure regions that cause the bubble to collapse. The resulting collapse can form highly concentrated microjets and shock waves that, when in close proximity to a solid surface, can cause serious damage over time. It is common to measure how close a fluid is to its vapor pressure (and therefore how likely it is to form cavitation bubbles) with its cavitation number which is defined as

$$\sigma = \frac{P_0 - P_{vapor}}{\frac{1}{2}U_{tip}^2} \tag{2.2}$$

where P_0 refers to the pressure upstream of the inducer, or at the inlet of the computational domain. The formation and collapse of cavitation bubbles in flows involving inducers can occur in many different forms. Significant work has been made to observe and understand the different modes of cavitation that occur in inducers. The most notable effect of cavitation on an inducer occurs when the cloud of cavitation around the blade grows so large that it essentially blocks the fluid from being able to flow through the inducer. When this happens, the inducer is said to be in "breakdown" and is accompanied by a drastic loss of head rise across the pump. Other common modes of cavitation include rotating cavitation, alternate-blade cavitation, vortex cavitation, and cavitation surge.

Rotating and alternate-blade cavitation instabilities are cavitation formations where the length of cavitation differs from one blade to another. When the vapor cavities grow large enough, the flow near the cavitation along one blade decreases the incidence at the leading edge of the next blade (see figure 2.1). This causes the next blade's cavity to shrink and results in unbalanced

cavitation across all the blades. For a four-bladed inducer, because there are an even number of blades, the process results in a steady alternate-blade cavitation formation [8]. For a three-bladed inducers, it results in an unsteady cavity pattern with the minimized cavity usually rotating super-synchronously from one blade surface to the next [9].

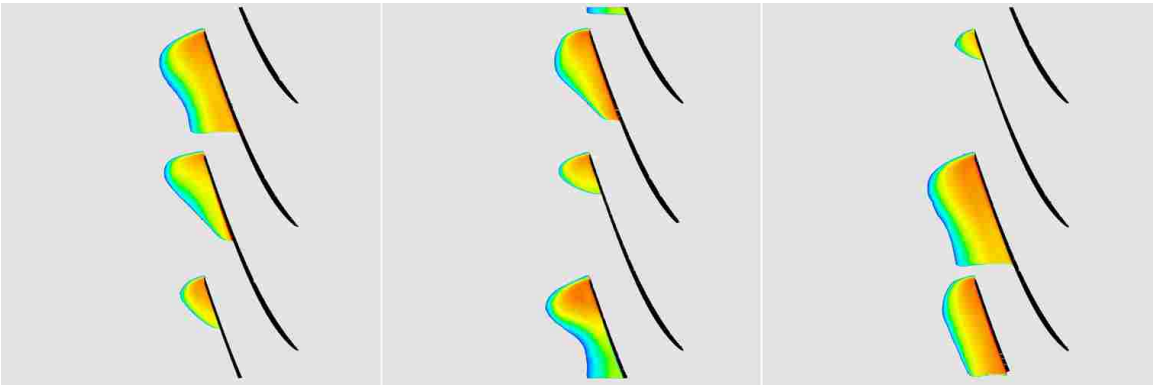

Figure 2.1: Contour plots of volume fraction of vapor at 98% span on a three-blade inducer. Rotating cavitation is shown in sequence of three images. Smaller cavitation bubble rotates to each blade.

Vortex cavitation refers to cavitation that develops along a vortex that occurs at the tip of the leading edge of the blade (see figure 2.2). Vortex cavitation is usually associated with the inception of cavitation, and is therefore commonly looked at when trying to suppress cavitation-caused instabilities [10].

Cavitation surge refers to the oscillatory growth and collapse of the vapor cavity within the inducer domain. A 1-D stability analysis performed by Tsujimoto et al. shows the mechanism that controls the cavitation surge. [8]. A simple velocity triangle shows that when the flow rate is increased, the incidence angle α decreases. If the mass flow gain factor $M = \partial(\forall_c/h^2)/\partial\alpha > 0$, then the cavity volume must also decrease and the upstream flow rate must increase even further in order to conserve mass. This positive feedback system is stabilized by the positive cavitation compliance of the fluid. The increasing flow rate causes the local static pressure to drop in the amount of the increased dynamic head. If the cavitation compliance $K = -\partial(\forall_c/h^2)/\partial\sigma > 0$, then the cavity volume must increase due to the decrease of the inlet pressure. It is this oscillation of cavity volume that is defined as cavitation surge.

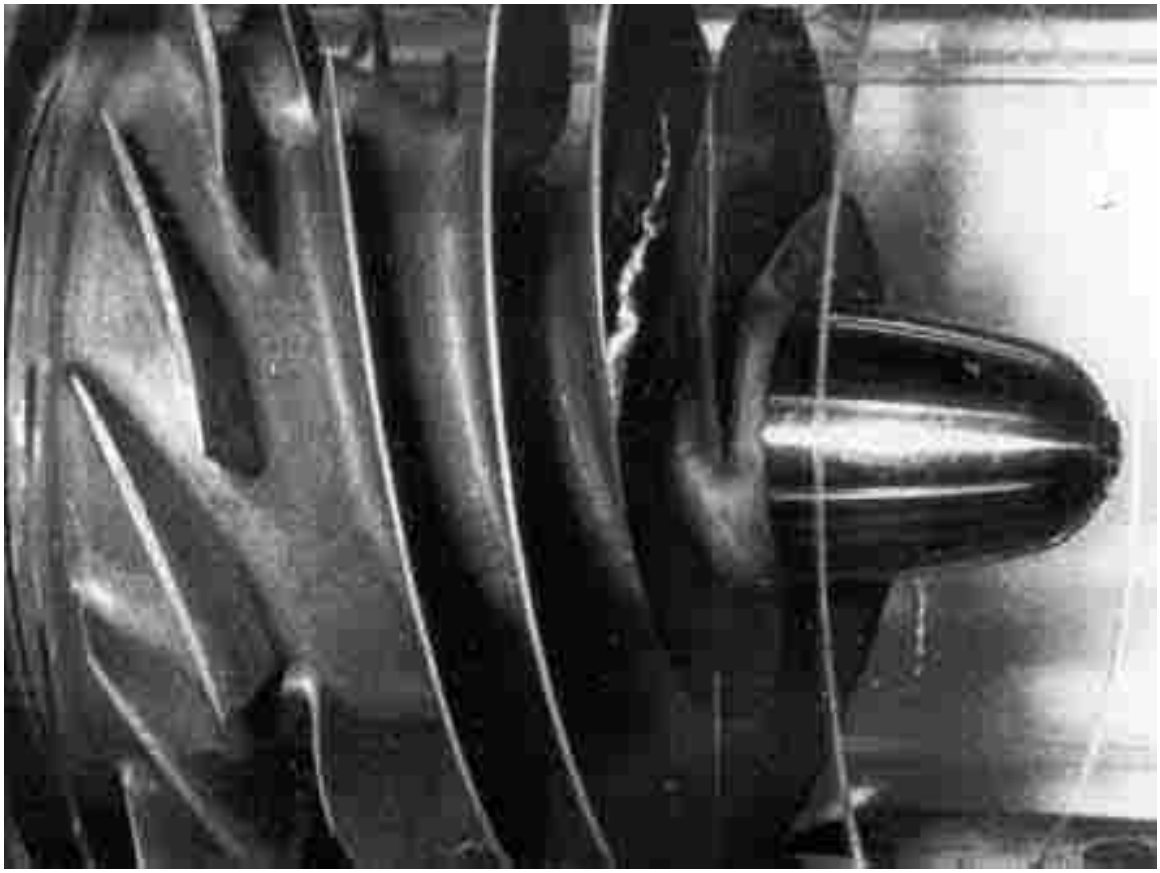

Figure 2.2: Tip vortex cavitation on Impeller. Image taken from Brennen [2]

2.3 Review of Cavitation Suppression Devices

There has been some prior research done on methods to reduce and control the amount of cavitation that forms on inducers. In 2001, Acosta et. al. [11] investigated the effects of leading edge sweep on the cavitating characteristics of inducer pumps. Three inducers with varying sweep angles of 90° (no sweep), a forward sweep of 25°, and a backward sweep of 47.3°. Cavity length was measured for varying values of cavitation number and incidence at the leading edge. It was shown both theoretically and experimentally that cavitation development was greatly delayed for both the forward and backward swept leading edges as compared to the base design of a leading edge of 90°.

In order to further understand and attempt to suppress the development of vortex cavitation, Chang et. al. [12] investigated methods to suppress vortex cavitation by use of active mass injection. An elliptical planform hydrofoil with a modified NACA 66 profile as reported by Platzer and

Sounders [13] was installed in a water tunnel for testing. A port was fabricated at the end of the hydrofoil's tip which allowed for aqueous solutions to be injected directly to the flow at the blade tip. A comparison was done between the base condition (no injection) and conditions with varying amounts of polymer/water solutions as well as at varying injection flow rates. For each condition, the cavitation number at which cavitation inception and development occurred was recorded. It was shown that injecting the flow greatly reduced the cavitation number at which cavitation began by as much as $\Delta\sigma = 1.2$, and the point of developed cavitation by $\Delta\sigma = 0.3$. Further investigation showed that increasing the polymer concentration in the solution also helped to reduce the points at which cavitation started and developed by an additional $\Delta\sigma = 1.2$(total improvement of 45%) and $\Delta\sigma = 0.7$ respectively.

Phase I [3] of this project studied the effects of a (SCD) on a flat-plate inducer. The same inducer at the same operating conditions were compared with one having the SCD installed and the other without. Figure 2.3 shows the velocity contours of a longitudinal cross-section of both simulations. It was observed that the significant backflow present at the tip of the leading edge for the inducer without the SCD was successfully removed for the inducer with the SCD. Additionally, it was shown that with the SCD installed, the flat-plate inducer was able to function at operating conditions well beyond the limits of the inducer without the SCD, due to its ability to locally increase the flow coefficient to that at which the inducer can successfully operate.

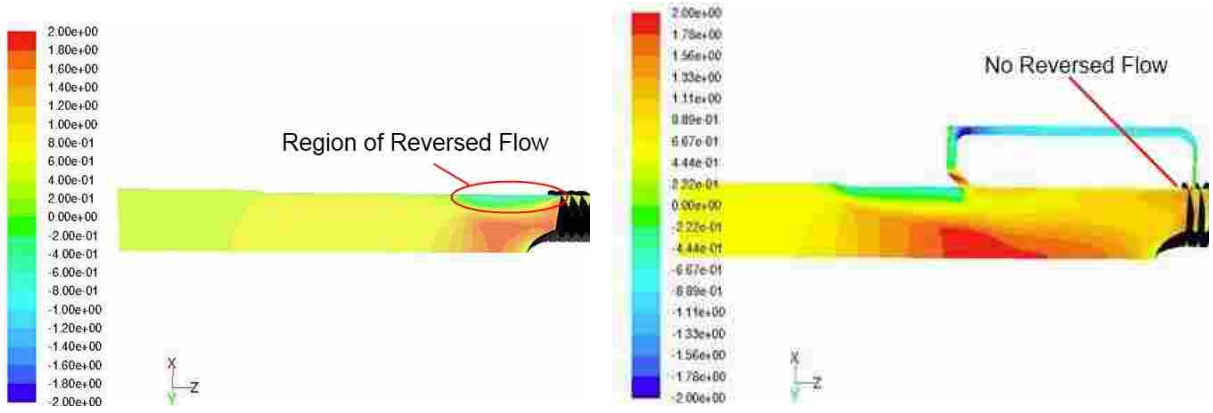

(a) Without SCD (b) With SCD

Figure 2.3: Velocity contours of 2.3(a) without the SCD and 2.3(b) with the SCD [3]

CHAPTER 3. PROCEDURE

3.1 Design Variables

This research involves comparing the performance of inducers with varying geometry configurations. In order to make the comparison several design variables will be used. These include head coefficient (ψ), efficiency (η), and mass flow gain ($\dot{m}_{gain}$). These design variables are defined in equations 3.1 thru 3.3 respectively.

$$\psi = \frac{P_{08} - P_{00}}{\rho U^2} \tag{3.1}$$

Head coefficient (ψ) is defined in equation 3.1 where P_{08} the total pressure of the outlet of the domain, P_{00} is the inlet total pressure, and ρ is the density of the liquid. For this application, water was the working fluid with a density of $\rho = 998.2^{kg}/_{m^3}$. P_{08} and P_{00} were calculated at the outlet and inlet geometry surfaces respectively. For reference of these surfaces, see figure 3.1. And finally, U_{tip} was calculated as the maximum velocity on the rotor. The head coefficient is used to measure the non-dimensional head rise of the pump and is used widely in the turbomachinery industry. In this research a normalized head coefficient may be used. Unless otherwise specified, the normalized head coefficient is defined as the head coefficient divided by the head coefficient of the baseline geometry at 100% flow (I7no inducer at $\phi = 0.07$). The purpose of the normalized head coefficient is to be able to compare performance between the inducers on a relative basis.

$$\begin{aligned} \eta &= \frac{w_{ideal}}{w_{actual}} \\ &= \frac{\dot{m}_{00} * \frac{P_{02} - P_{00}}{\rho}}{T * \Omega} \end{aligned} \tag{3.2}$$

Efficiency (η) is defined in equation 3.2 where w_{ideal} is the ideal work input to the machine and w_{actual} is the actual work input to the machine. $\dot{m}_{00}$ is the mass flux at the inlet and P_{02} is the total pressures at the trailing edge of the inducer. T is the torque calculated on the rotor and Ω is the angular velocity of the rotor, which in this research is a constant 628.3 $^{rad}/_{s}$. Efficiency is a measure of how well the machine is able to convert the input (torque) into the desired output (head rise).

$$\dot{m}_{gain} = \frac{\dot{m}_{01}}{\dot{m}_{00}} \tag{3.3}$$

Mass flow gain ($\dot{m}_{gain}$) is defined in equation 3.3 where $\dot{m}_{01}$ is the local mass flow at the inducer leading edge and $\dot{m}_{00}$ is the local mass flow at the inlet. Mass flow gain provides insight to how much recirculation occurs through the SCD. As part of this research, it will be shown how mass flow gain is linked with the other design variables (head rise and efficiency).

3.2 Geometries

All geometries used in this research were provided by ConceptsNREC. All geometries used were variations of the same "baseline" geometry (see figure 3.1). The baseline geometry consisted of a circular inlet approximaetly 6.5 diameters (0.88m) from the leading edge of the inducer. The shroud is non-tapered and cylindrical. The SCD is seen as the recirculation duct with its outlet approximately 1.5 diameters (0.2m) upstream of the leading edge and inlet in the center of the inducer blade region. The outlet is annular in shape, created by the rotor hub and shroud, approximately 2.2 diameters (0.3m) from the leading edge. Most geometry variations were the inlet blade angle and blade solidity (for the baseline geometry, inlet blade angle was 7° and the solidity was 2.09). The details of those variations are explained in table 3.1.

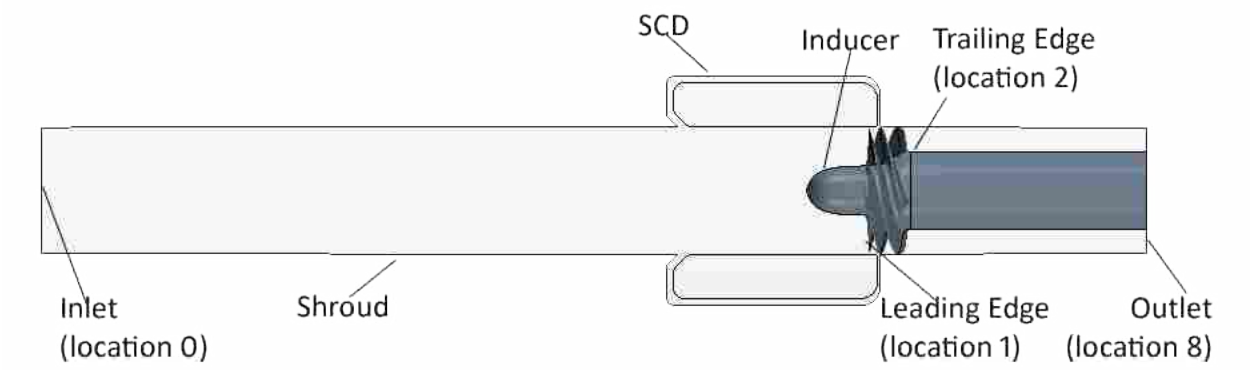

Figure 3.1: Side view of baseline geometry with SCD

Table 3.1: Geometry Information

Name	Inlet Tip Blade Angle	Description
I7	7°	Baseline Geometry
I7opt	7°	I7 with optimized SCD
I7no	7°	I7 without SCD
I9	9°	Same Solidity as I7
I11	11°	Same Solidity as I7
I14	14°	Same Solidity as I7
I14s	14°	Same Axial Length as I7
Four-Bladed	7°	Baseline geometry, used in unsteady simulations
Three-Bladed	7°	Same as baseline except with 3 blades instead of 4

3.3 Explanation of Varying Parameters

The majority of this research involved running CFD simulations using the same baseline inducer geometry while varying the following parameters: number of blades, with or without SCD, flow coefficient, cavitation number, and the leading edge blade angle.

3.3.1 Number of Blades

The initial stages of this research involved a comparison between a three-bladed and four-bladed inducer. Two-phase unsteady simulations were run on identical inducer geometries that only varied in the number of blades they had: one with three blades and the other with four. In order to fully analyze the performance of the two inducer configurations and make a valid comparison, the simulations also varied flow coefficient and inlet pressure for each of the two configurations.

3.3.2 SCD Attachment

Some simulations were run with an inducer configuration without the SCD attached. This served as a control to show the effects the SCD has on the machine.

3.3.3 Flow Coefficient

Varying the flow coefficient demonstrates the operating range robustness of the inducer. Reduced flow coefficients have the effect of increasing the incidence angle which generally both increases head while at the same making the machine more susceptible to cavitation inception. One of the benefits of the SCD is to reduce the change of the incidence angle when operating at low flow coefficients. This helps the machine to operate more stably at off-design flow coefficients.

3.3.4 Cavitation Number

Cavitation number was controlled by changing the inlet pressure of the fluid. By changing the cavitation number, it is possible to create a pump's breakdown curve which shows the operating limit of the pump in terms of inlet pressure.

3.3.5 Leading Edge Blade Angle

All other parameters held constant, changing the leading edge blade angle affects the inlet incidence angle. Part of this research was designed to compare inducers with different inlet blade angles with a SCD.

3.4 CFD Setup

The CFD setup is described in chapters 4 and 5 for their respective simulations.

3.5 CFD Validation Case

Validation of the CFD setup was performed by comparing experimental data with the CFD simulations for the I7 and I7no configurations at design and 60% flow rates. Experimental tests

were performed and data provided by ConceptsNREC. Figure 3.2 shows normalized head rise as a function of cavitation number for the I7 and I7no configurations at 100% and 60% flow rates.

The I7 at 100% flow case tracked the experimental data very well. For the cavitation numbers in the region of constant head rise, the error in head rise between the simulation results and the experimental data varied between 1.7% and 2.2%. The estimation of the breakdown point for the simulation results and the experimental data were at cavitation numbers of $\sigma = 0.025$ and $\sigma = 0.028$ respectively.

The I7 at 60% flow case also tracked the experimental data very well, but with a slightly under-prediction of head rise. For the cavitation numbers in the region of constant head rise, the error in head rise between the simulation results and the experimental data varied between 4.3% and 6.7%. The estimation of the breakdown point for the simulation results and the experimental data were at cavitation numbers of $\sigma = 0.014$ and $\sigma = 0.018$ respectively.

The I7no at 100% flow case tracked the experimental data pretty well, but tended to have a higher head rise than did the experimental data. For the cavitation numbers in the region of constant head rise, the error in head rise between the simulation results and the experimental data varied between 8.2% and 11.8%. The estimation of the breakdown point for the simulation results and the experimental data were at cavitation numbers of $\sigma = 0.025$ and $\sigma = 0.024$ respectively.

The I7no at 60% flow case seemed to track the experimental data the worst, however, it did track it pretty well and the experimental data for this case also showed the most variation out of all the cases. For the cavitation numbers in the region of constant head rise, the error in head rise between the simulation results and the experimental data varied between 2.2% and 9.0%. The estimation of the breakdown point for the simulation results and the experimental data were at cavitation numbers of $\sigma = 0.043$ and $\sigma = 0.024$ respectively.

Overall, the head rise and breakdown points tracked very well between the CFD results and the experimental results. It's important to note that this research focused on comparing CFD simulations to other CFD simulations of the same setup, and because the breakdown profiles matched the experimental data very well, it is believed that the CFD setup was valid for purposes of this research.

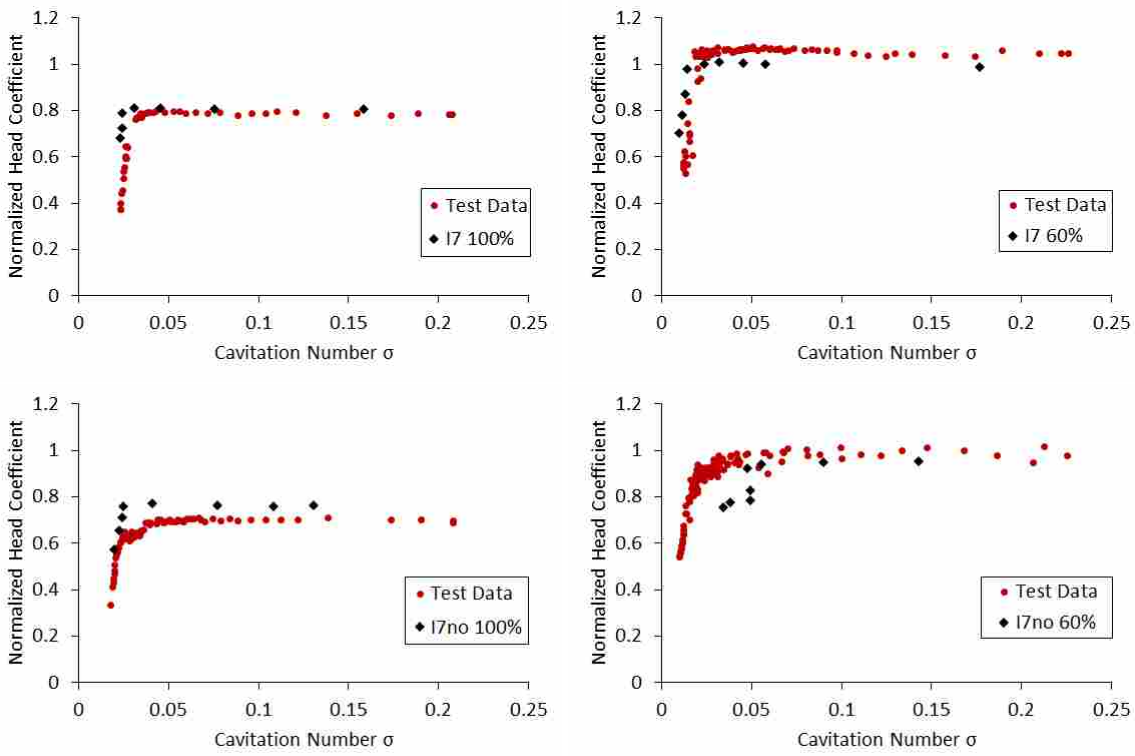

Figure 3.2: Normalized head coefficient as a function of cavitation number for the I7 and I7no inducers at 100% and 60% flow rates with experimental data for comparison

3.6 Data Analysis

The CFD results were analyzed by employing many of Star-CCM+'s built-in tools including its report, monitor, plot, and scene features. These tools make it possible to make detailed calculations of the desired performance metric based on the pressure and velocity results of the simulation, and then to display those calculations in multiple ways including x-y scatter plots and contour plots. Many of the calculations were made by creating derived parts (also known as iso-parts) that represent cross-sectional slices at specific axial locations (such as the inducer inlet and exit).

3.6.1 Single Calculations

Once a simulations has converged, these calculations return a single value that measure the inducer at given moment in time (unsteady simulations) or at its steady state (steady simulations).

For unsteady simulations, these calculations are plotted on x-y scatter plots with the time step along the x-axis.

Vapor Fraction

For the two-phase unsteady simulations, vapor fraction was calculated. This calculation is useful to compare total magnitude of cavitation within the domain. This same report is also used in the vapor fraction contour plot, which will be discussed later. The vapor fraction is calculated as the volume fraction of water vapor within the entire domain.

3.6.2 Traverse Plots

To better view the incidence angle and axial velocity, traverse plots were generated. In these plots, the variable is displayed along the x-axis as a function of blade span along the y-axis. This helps to show how the variable changes along the blade. Generally, the data used to generate a traverse plot comes from a cross-sectional surface at a specific axial location (such as blade leading edge). Figure 3.3 shows an example of a traverse plot, displaying blade span as a function of incidence for the I7 and I7no inducers at $\phi = 0.028$.

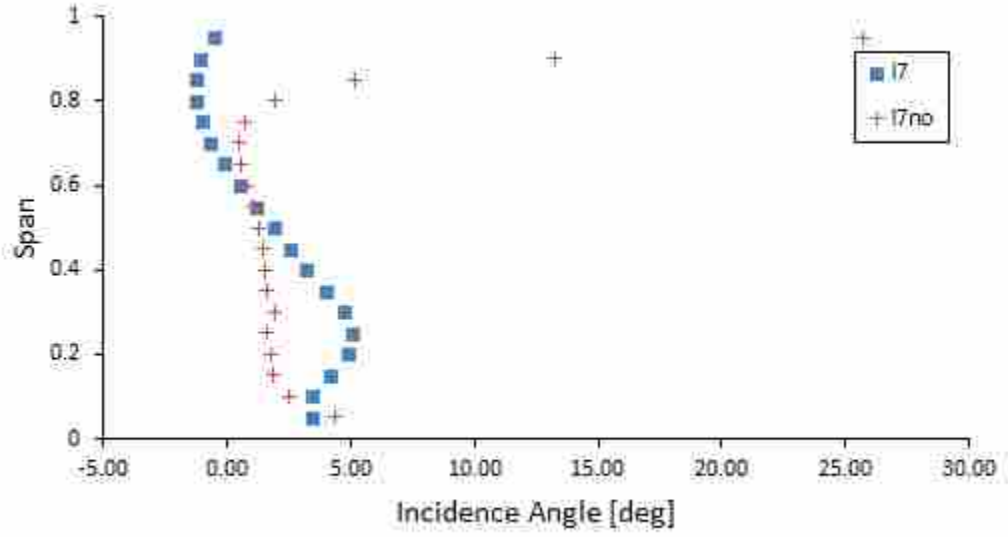

Figure 3.3: Traverse plot of incidence comparing I7no and I7 at $\phi = 0.028$

Incidence Angle

Incidence was calculated based on the relationships shown in figure 3.4

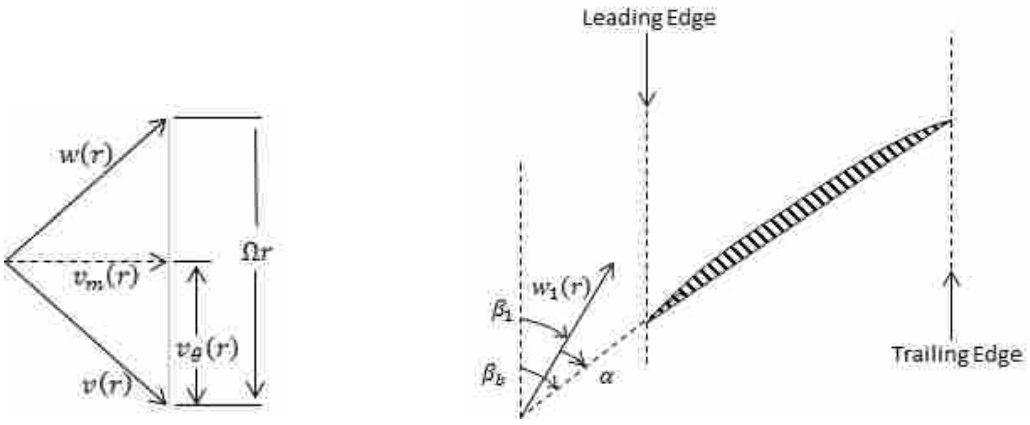

Figure 3.4: Diagram on left gives the velocity triangle showing relationship of flow velocity ($v(r)$), meridional velocity ($v_m(r)$), relative velocity ($w(r)$), angular velocity ($v_\theta(r)$), and blade velocity (Ωr). Diagram on right gives geometric representation of the incidence angle

Tsujimoto pointed out that increased incidence angles lead to an increase in cavitation, and once the cavity length to blade spacing ratio (l_s/h) approaches nominally 0.65, instability modes such as rotating and alternate-blade cavitation begin to develop [8]. Brennen recommends maintaining a nominal incidence angle of $+2^\circ$ in order to ensure the suction side of the blade doesn't change [2]. To see how incidence changes at different span locations, a traverse plot was used at the leading edge of the inducer (location 01 in figure 3.1). Data was gathered and averaged circumferentially at 20 radial "buckets" distributed uniformly along the blade span. These "buckets" are the data points shown in the sample figure 3.3.

Axial Velocity

Similar to incidence, axial velocity was analyzed using traverse plots. The analysis was done at the leading edge axial location (location 01 on figure 3.1). Also similar to incidence, axial velocity values were averaged circumferentially in 20 radial "buckets" distributed uniformly along the blade span.

3.6.3 Rotor Forces

To show the forces on the rotor shaft over time, an orbit plot was used. The x and y axes represent the magnitude of force in the x and y direction (according to the coordinate system in Star-CCM+). Both the x and y directions face radially and are orthogonal to each other. Imagine you are upstream of the inducer and looking down at the nose. Each data point represents the x and y components of the force experienced by the shaft of the rotor at a given point in time. The orbit plot helps to show the variability of force over time on the rotor shaft. Figure 3.5 is an example of an orbit plot of forces on the I7 inducer at $\phi = 0.042$ and $\sigma = 0.015$.

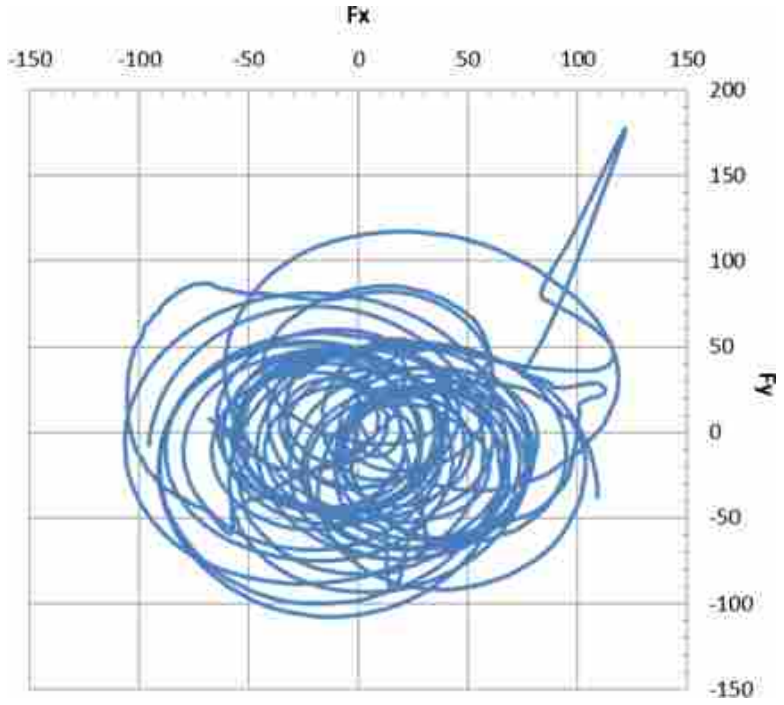

Figure 3.5: Orbit forces plot of I7 at $\phi = 0.042$ and $\sigma = 0.015$

3.6.4 Contour Plots

When it was necessary to look at variables along a surface or a 2-D extract, contour plots were used. These plots show a 2-d surface and are colored with a gradient to visually show the variable's values throughout the surface. Figure 3.6 provides an example of a contour plot of total pressure for the I7 inducer. Contour plots were used to visualize many variables to help understand

the flow dynamics within the inducer. Particularly, contour plots of vapor fraction (precentage of vapor at a given cell), pressure (total and static), and velocity (magnitude and directional) were often employed.

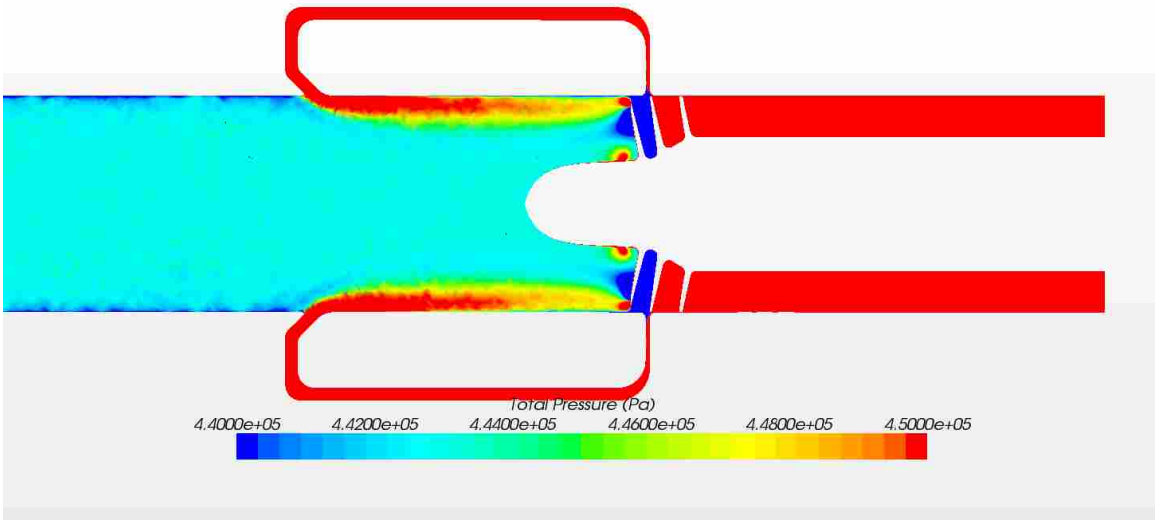

Figure 3.6: Contour plot of total pressure of I7 at $\phi = 0.07$ and $\sigma = 0.497$

CHAPTER 4. A COMPARISON OF THREE-BLADED AND FOUR-BLADED INDUCERS AT ON AND OFF DESIGN FLOW RATES

4.1 Contributing Authors and Affiliations

Ryan C. Cluff, Ryan K. Lundgreen, Steven E. Gorrell, R. Daniel Maynes
Department of Mechanical Engineering, Brigham Young University, Provo, UT 84602

Kerry Oliphant
Concepts NREC, White River Junction, VT. 05001, USA

4.2 Abstract

A computational fluid dynamic comparison was performed between on-design and off-design flow rates through a four-bladed and a three-bladed axial pump inducer. The simulations were time-resolved two phases (water and water vapor). Turbulence modeling employed the realizable k-ε model and cavitation was predicted using the Rayleigh-Plesset model. The solution discretization is second order accurate in space and first order accurate in time. The results show classical breakdown curves for all four cases. The purpose of this paper is to compare performance behaviors between a three-bladed and four-bladed inducer operating at on-design and off-design flow rates. Certain rotating instabilities have previously been observed with the four-bladed inducer and we investigate whether similar instabilities exist for a three-bladed geometry. We also investigate how off-design operation affects the stability of both inducer geometries. At design flow rates, there were very small differences between the breakdown curves for the three and four-bladed inducers. However, at lower cavitation numbers, the three-bladed inducer exhibited up to three times the rotor forces than the four-bladed inducer. When moving to off-design flow rates, both inducers experienced multiple modes of cavitation instabilities including rotating cavitation, alternate-blade cavitation, and cavitation surge. The four-bladed inducer began experiencing the

[1]This chapter is a manuscript presented at the 49th American Institute of Aeronautics and Astronautics Joint Propulsion Conference (AIAA Paper 2013-3761). The formatting of the paper has been modified to meet the stylistic requirements of this thesis.

formation of these modes of instability beginning at a cavitation number of $\sigma = 0.047$ whereas the three-bladed inducer began at a cavitation number of $\sigma = 0.091$. Additionally, the three-bladed inducer showed rotor forces up to ten times higher than the four-bladed inducer at similar cavitation numbers.

4.3 Nomenclature

$$\phi = \frac{Q}{AU_{tip}}$$
$$\sigma = \frac{P_{01} - P_v}{\frac{1}{2}\rho U_{tip}^2}$$
$$\psi = \frac{P_{08} - P_{00}}{\rho U_{tip}^2}$$
$$NPSH = \left(\frac{P_1}{\rho g} + \frac{V_1^2}{2g}\right) - \frac{\rho_v}{\rho g}$$
$$NSS = \frac{N\sqrt{Q}}{NPSH^{0.75}}$$
$$CorrectedNSS = \frac{NSS}{(1 - (\frac{r_{1h}}{r_{1t}})^2)^{0.5}}$$
$$\alpha = \beta_b - \beta_1$$

α	Incidence Angle $[deg]$
β_1	Relative Velocity Flow Angle $[deg]$
β_b	Inlet Blade Angle $[deg]$
μ	Dynamic Viscosity $[m^2/s]$
ρ	Density $[kg/m^3]$
σ	Cavitation Number $[-]$
ϕ	Flow Coefficient $[-]$
ψ	Head Rise Coefficient $[-]$
A	Inlet Area $[m^2]$
g	Gravity $[m/s^2]$

h	Blade Spacing $[m]$
K	Cavitation Compliance $[-]$
M	Mass Flow Gain Factor $[-]$
$\dot{m}$	Mass Flow Rate $[kg/s]$
N	Rotational Speed of Pump$[Rpm]$
$NPSH$	Net Positive Suction Head $[m]$
Nss	Net Suction Specific Speed $[-]$
P	Local Static Pressure $[Pa]$
Q	Volumetric Flow Rate $[m^3/s]$
T	Torque $[n-m]$
U_{tip}	Blade Tip Speed $[m/s]$
V	Local Fluid Velocity $[m/s]$
$\forall$	Volume $[m^3]$

Subscripts, superscripts, and other indicators

$[\,]_0$	indicates [ ] is a property at the inlet of the domain
$[\,]_{0(\,)}$	indicates [ ] is a stagnation property according to the ( ) subscript
$[\,]_1$	indicates [ ] is a property at 2mm upstream of leading edge of inducer
$[\,]_2$	indicates [ ] is a property at 2mm downstream of trailing edge of inducer
$[\,]_C$	indicates [ ] is of the vapor cavity
$[\,]_{norm}$	indicates [ ] is normalized by the I7no inducer at 100% flow
$[\,]_v$	indicates [ ] is a property of the vapor state

4.4 Introduction

4.4.1 Background

Inducers

One of the primary factors that drives cost to develop space launch vehicles is the propellant feed system. The propellant feed system will typically have at least one pump that boosts the

propellant from a low pressure tank to the high pressure chamber injectors. Developing a pump with higher suction performance (having a lowered required NPSH) means a lower required propellant tank pressure which equates to lower weight and payload costs. High suction performance pumps are also critical in many other applications where it is advantageous to have low inlet pump pressures. These applications include boiler feed pumps, aircraft fuel pumps, and liquefied natural gas transfer pumps. The inlet portion of the pump impeller, or inducer, is a key component in determining the suction performance of the pump and is one of the most difficult components to design properly.

The role of the inducer is to raise the propellant's pressure to a level adequate to allow the downstream components to operate without the presence of cavitation. Cavitation refers to when a fluid's local pressure drops below its vapor pressure and vapor cavities form, normally along the suction side of the blade, which can lead to debilitating effects on the pump such as:

1. large reduction in head rise when the vapor cavity reaches the size of the inducer's inlet throat

2. blade damage caused by the growth and collapse of cavitation bubbles

3. blade structural failure and inconsistent mass flow rates. This can cause catastrophic changes in engine thrust and is generated by large instabilities due to the interaction between the flow and the vapor cavities.

Suction performance depends on minimizing the inlet bulk velocity of the flow. The inlet flow coefficient (ϕ) is directly related to the inlet bulk velocity. Figure 4.1 shows the relationship between suction performance and inlet flow coefficient by comparing several cold water tests of various inducers with the Brumfield criterion. The Brumfield criterion is the theoretical maximum suction performance possible at a given flow coefficient without any thermal suppression head effects (TSH) [4]. The general trend is that suction performance can be increased dramatically with small decreases in flow coefficient; however, in practice it is difficult to design an inducer that can run stably at flow coefficients below 0.06 [1].

At low flow coefficients, the relative flow angle begins to approach zero, and in order to maintain the design incidence of only a few degrees [2], the blade angle must also decrease and

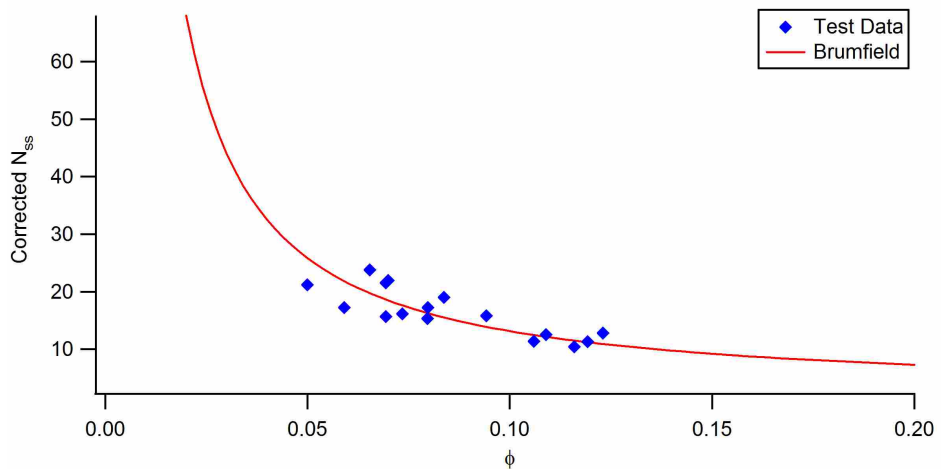

Figure 4.1: Corrected N_{ss} as a function of flow coefficient for various cold water inducer tests compared to Brumfield criterion [4]

approach zero. Small blade angles effectively reduce the inlet throat area which can expose the pump to premature breakdown. Efforts can be made to enlarge the throat area by reducing the blade thickness, however, this is done at the expense of reducing structural integrity. Additionally, small blade angles reduce the pump's tolerance to changes in incidence which restricts its ability to run at off-design flow coefficients. As mentioned earlier, there is a traditional limit on the flow coefficient that an inducer can be designed for. This limit is determined mostly by the instabilities that arise in low-flow environments. This paper will compare the instability characteristics between geometrically similar three-bladed and four-bladed inducers at on-design and off-design flow rates. The instabilities that we focused on include rotating and alternate blade cavitation, surging cavitation, and tip vortex structures and backflow.

Rotating and Alternate-Blade Cavitation

It has been shown that both rotating and alternate-blade cavitation instabilities tend to occur when the cavity length to blade spacing ratio (l_s/h) approaches nominally 0.65 [8]. When the vapor cavities grow large enough, the flow near the trailing edge of the longer cavity decreases the incidence at the leading edge of the next blade. This causes the next blade's cavity to shrink. For a four-bladed inducer, this process results in a steady alternate-blade cavitation formation [8];

whereas for a three-bladed inducer it results in an unsteady cavity pattern with the minimized cavity usually rotating supersynchronously from one blade surface to the next (see figure 4.9). [9]

Surging Cavitation

Cavitation surge refers to the oscillatory growth and collapse of the vapor cavity within the inducer domain. A 1-D stability analysis performed by Tsujimoto et al. shows the mechanism that controls the cavitation surge. [8]. A simple velocity triangle shows that when the flow rate is increased, the incidence angle α decreases. If the mass flow gain factor $M = \partial(\forall_c / h^2)/\partial\alpha > 0$, then the cavity volume must also decrease and the upstream flow rate must increase even further in order to conserve mass. This positive feedback system is stabilized by the positive cavitation compliance of the fluid. The increasing flow rate causes the local static pressure to drop in the amount of the increased dynamic head. If the cavitation compliance $K = -\partial(\forall_c / h^2)/\partial\sigma > 0$, then the cavity volume must increase due to the decrease of the inlet pressure. It is this oscillation of cavity volume that we reference as cavitation surge (see figure 4.8).

Tip Vortex Structures & Backflow

Although not as influential as surging and alternate/rotating cavitation, weaker higher-order cavitation instabilities have been observed. Some higher-order modes measured by Tsujimoto et al. show pressure fluctuations close to the same frequency as the first bending mode of blade vibration [9], and therefore are important to address. Work done by Kang et al. suggests that the higher frequency components are caused by the interaction of the backflow vortices with the blades [14]. Backflow vortices are vortices of reverse flow that form at the tip of the blade leading edge that can cause cavitation. Tip vortex cavitation is usually associated with the inception of cavitation.

4.4.2 Motivation

The ability to operate stably at low flow coefficients is key to achieving a pump with high suction performance. There has been significant debate over the benefits and drawbacks between three-bladed and four-bladed inducers. Many publications have appeared that have analyzed the

performance and stability of these two inducer genres, yet there hasn't been much in directly comparing the two in similar environments. In hopes of providing further insight to this comparison, the purpose of this paper is to present a CFD analysis of the instabilities present in geometrically similar three-bladed and four-bladed inducers at on-design and off-design flow rates, and to discuss how those instabilities affect the overall pump performance.

4.5 Geometry

This study investigates the performance of two inducer geometries. Both geometries are similar with a tapered leading edge, a tip blade angle of 7°, and a design point flow coefficient of $\phi = 0.07$. Both have a hub radius of $41mm$ and tip blade radius of $67mm$. They differ only in the blade count. One is a three-bladed and the other is a four-bladed inducer as shown in Figure 4.2.

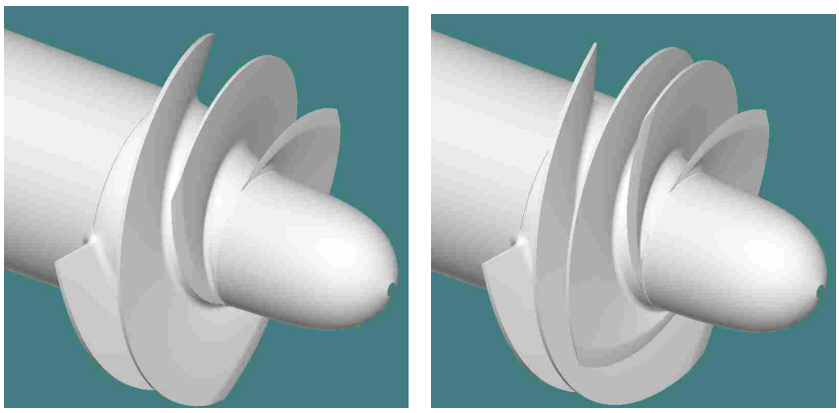

(a) Three-bladed Geometry (b) Four-bladed Geometry

Figure 4.2: Images of similar three and four-blade inducer geometries. Both geometries share the same basic design.

4.6 Methods

4.6.1 CFD Simulation

Solver

CD-adapco's STAR-CCM+ v7 was the solver used in this study. Simulations were run in a two-phase unsteady environment using STAR-CCM+'s VOF(Volume of Fluid) multiphase model. Water and water vapor were used as the liquid and vapor phases respectively. Turbulence effects were estimated using the Realizable k-ε two-layer model. The two-layer approach allows the k-ε model to be applied to the viscous sublayer. In this approach, the computation is divided into two layers. The near-wall layer's turbulent dissipation rate ε and turbulent viscosity μ are specified as functions of the wall distance and are blended with the values computed from solving the transport equation far from the wall. The velocity and pressure flow equations were solved using STAR-CCM+'s Segregated Flow solver which solves them in an uncoupled manner and updates the flow field using a SIMPLE-type algorithm. The solver accuracy was 2^{nd} order in space and 1^{st} order in time.

STAR-CCM+'s cavitation model was used to describe the multiphase interaction. In the model, it is assumed that all vapor bubbles in a control volume have the same radius and a homogeneous distribution. This allows us to describe the bubble distribution by a single scalar field (vapor volume fraction α_v). Bubble nucleation is initiated by micro-bubbles or "seeds" that pre-exist within the fluid and whose diameter and density are defined by the model. The default diameter and density values of $1 \times 10^{-6} m$ and $1 \times 10^{12} seeds/m^3$, which were designed to simulate cavitating water, were used. The cavitation bubble growth rate is estimated using the inertia controlled growth model which is a simplification of the more general Rayleigh-Plesset equation. The simplification involves omitting the viscous and surface tension effects [15].

Grid Generation

A mesh of the domain was created using STAR-CCM+'s internal meshing tool. The geometries were first created on a CAD package and imported to STAR-CCM+ in the STP format. We employed STAR-CCM+'s polyhedral and prism-layer meshing models. The polyhedral mesher

generated polyhedral cells throughout the domain. The prism-layer mesher created 3 prism layers near the surface boundaries in order to improve the accuracy of the boundary-layer approximations. For the four-bladed geometry, a total of 6,446,655 cells were generated, and for the three-bladed geometry, a total of 4,964,850 cells were generated. In order to better capture cavitation and its effects, a finer grid was necessary for the region near the inducer blades. A conical volumetric control (Figure 4.3) was created to refine the mesh in the region near the inducer blades. Within this region, the target cell size was reduced by 80% and the number of prism layers was increased from 3 to 10 layers. The increased resolution near the inducer blades resulted in an acceptable maximum Wall y^+ value of 70 and an average Wall y^+ value of 17. Low y^+ values allow for a wall-treatment that assumes the viscous sublayer is properly resolved [15]. High y^+ values (above 100) rely on a wall-function approach that approximates the viscous sublayer effects and assumes the near-wall cell lies within the logarithmic region of the boundary layer. Our simulations employed an all-y^+ wall treatment [15] which is a hybrid treatment that attempts to emulate the high y^+ wall treatment for coarse meshes and the low y^+ treatment for fine meshes.

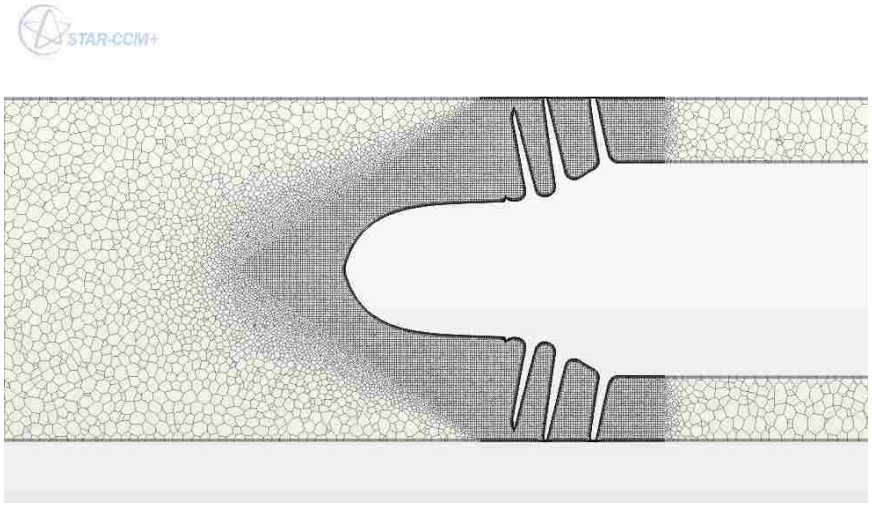

Figure 4.3: Lengthwise cross section showing mesh generated for four-bladed inducer. Conical volumetric control allows for refined mesh near inducer blades.

Boundary Conditions

The domain was specified as a rotating relative reference frame at 6,000 rpm. The shroud and rotor were set as no-slip boundary walls with the rotor fixed to the rotating reference frame and the shroud fixed to be stationary to the absolute reference frame. The inlet boundary was set as a mass-flow inlet, where the mass flux normal to the inlet surface may be controlled. The outlet boundary was set as a radial-equilibrium pressure outlet, where the pressure at the hub may be controlled.

Grid Independence

To determine grid independence, two meshes were generated for a slightly different four-bladed geometry. The coarser of the two contained 6,667,204 cells and the finer mesh contained 12,199,553 cells. A critical parameter in determining pump performance is the head coefficient, ψ. Both simulations were run to convergence and we compared their head coefficients averaged over the equivalent to 10 rotor revolutions. With a difference of approximately 0.34%, we determined the coarser of the two meshes to be adequate for our purposes.

Convergence

Convergence was determined in a case by case basis based on the following criteria:

1. residuals were showing a stable behavior. Stable behavior is characterized by residuals dropping and becoming level for each time step, and overall residual levels are unchanging

2. monitors for the domain's inlet pressure (P_0), the inducer's exit pressure (P_2), the rotor's torque, and the domain's volume fraction of vapor were either periodic or flat and unchanging. In general, we would compare the average monitor value calculated over 5 rotor revolutions to the average monitor value calculated over 10 revolutions. If the error was less than 2%, it was considered converged.

4.7 Results

In order to compare the three-blade and four-blade inducers, the respective head breakdown curves were considered. A head breakdown curve is useful to show how a pump's head rise will behave as a function of cavitation number. The breakdown curve alone, however, is insufficient. If the instabilities are too severe, it is possible for a pump to fail even before the point of breakdown is reached due to unbalanced loads on the rotor. We therefore also considered the rotor loads experienced by the two inducers as well as the occurrences of different instability modes observed in the simulations.

4.7.1 Pump Performance Curves

Figure 4.4 shows how the normalized head coefficient ψ_{norm} varies as a function of cavitation number σ for both inducers at 100% and 60% flow rates.

At design flow coefficient, ψ_{norm} for both the three-bladed and four-bladed inducers follow a similar curve. The non-cavitating normalized head coefficient for both inducers is $\psi_{norm} = 1.0$. If we define the point of breakdown as the cavitation number where the head rise is 95% of the non-cavitating head rise,then they both begin breakdown at a cavitation number of $\sigma \approx 0.025$.

At 60% flow coefficient, the four-bladed inducer exhibits a higher non-cavitating head rise than the three-bladed inducer ($\psi_{norm} = 1.42$ for the four-blade compared to $\psi_{norm} = 1.33$ for the three-blade). Additionally, the four-bladed inducer begins breakdown at a cavitation number of $\sigma \approx 0.039$ while the three-bladed inducer has an earlier and more gradual breakdown starting at a cavitation number of about $\sigma \approx 0.05$.

4.7.2 Rotor Forces

Figure 4.5 shows the normalized maximum rotor force applied to the three-bladed and four-bladed inducers at design flow. Normalized force was calculated by dividing rotor force by the four-blade at 100% flow and a cavitation number of $\sigma = 0.132$. Both inducers experience low rotor forces for non-cavitating cases and a significant rise in rotor forces just before breakdown ($0.03 < \sigma < 0.05$). In this region, the rotor force for the three-blade inducer is nearly three times larger than the force for the four-bladed inducer (at $\sigma = 0.041$ the four-bladed inducer has a maximum

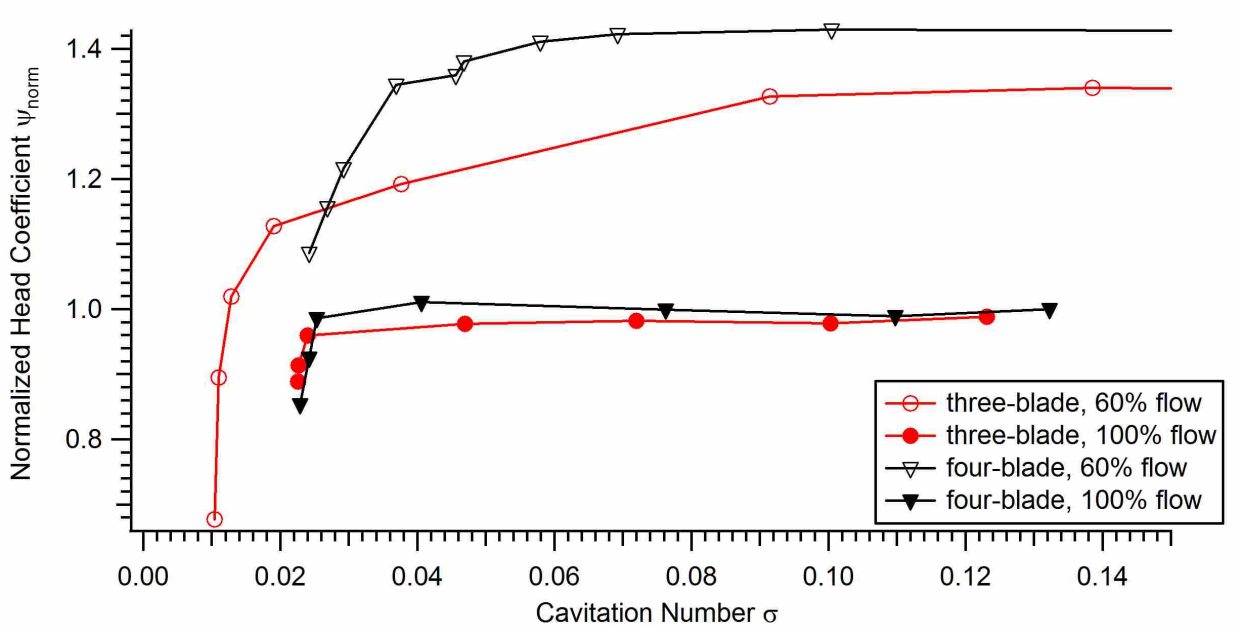

Figure 4.4: Head Coefficient (ψ), normalized by the on-design four-blade non-cavitating case, as a function of cavitation number (σ) for three-blade and four-blade inducers at 100% and 60% flow.

normalized force of 30.2 while the three-bladed inducer has a maximum normalized force of 94.5 at a higher cavitation number of $\sigma = 0.047$, a factor of 3 increase). Once breakdown is reached, rotor forces fall back down to lower values (between 0 and 20).

For the off-design cases, the detrimental impact that instabilities have on the rotor forces becomes manifest. Figure 4.6 shows the normalized maximum rotor force applied to the three and four-bladed inducers at 60% flow. At this off-design flow rate, the four-bladed inducer behaved much more stably than the three-blade for cavitation numbers higher than $\sigma = 0.04$. At higher cavitation numbers, the four-blade inducer has forces comparable to those found in the on-design cases while the three-blade inducer exhibits extremely high forces even at fairly high cavitation numbers. For example, at a cavitation number of $\sigma \approx 0.10$, the four-blade inducer has a normalized maximum rotor force of 6.42, and the three-blade inducer at a higher cavitation number of $\sigma \approx 0.139$ has a normalized maximum rotor force of 126.6. At lower cavitation numbers ($\sigma < 0.04$), the forces experienced by the four-blade inducer increase to match those of the three-blade. A consideration of the instabilities that exist for these cavitation numbers reveals an explanation for the sudden increase in forces for the four-blade inducer and is discussed later in this section.

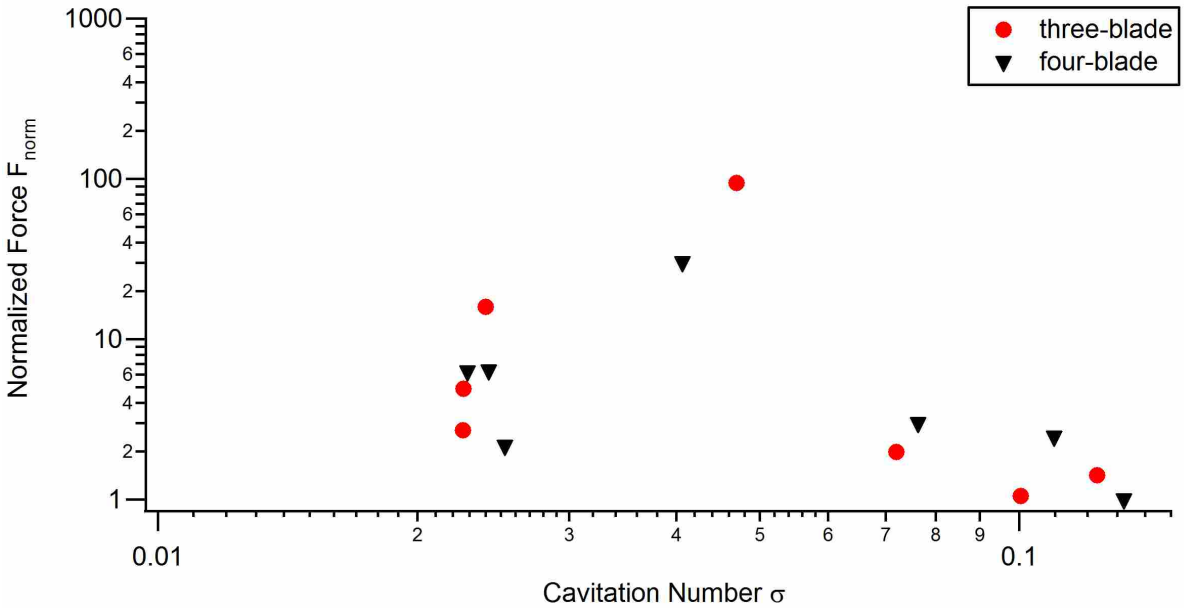

Figure 4.5: Maximum rotor force, normalized by the on-design four-blade non-cavitating case, as a function of cavitation number (σ) for three-blade and four-blade inducers at 100% flow.

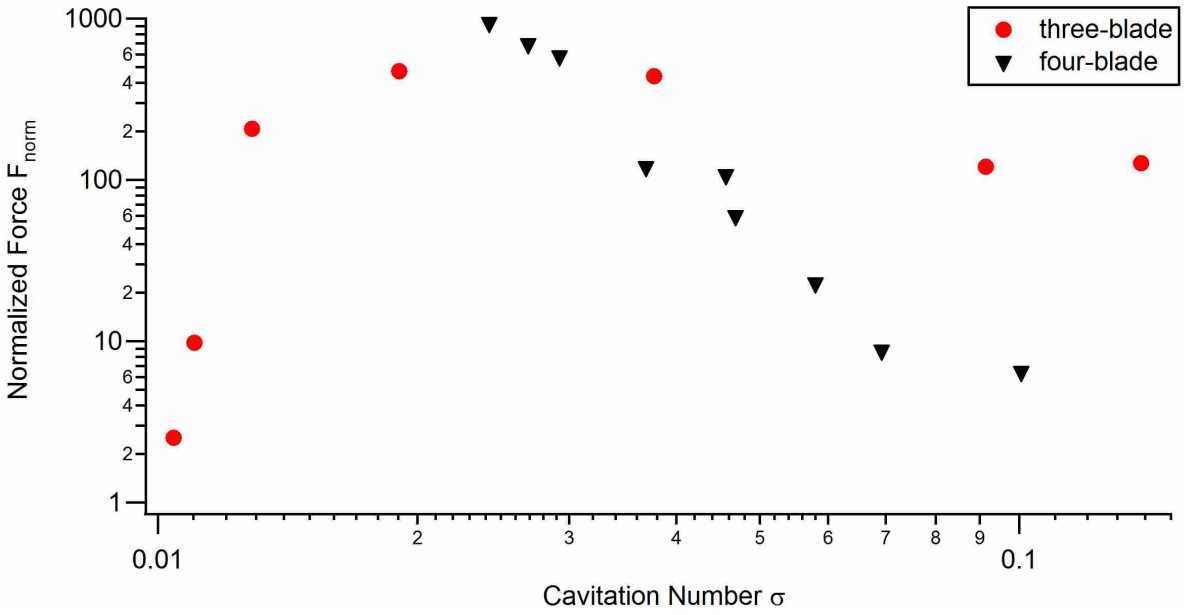

Figure 4.6: Maximum rotor force, normalized by the on-design four-blade non-cavitating case, as a function of cavitation number (σ) for three-blade and four-blade inducers at 60% flow.

4.7.3 Observed Instabilities

Many of the common cavitation instabilities have been observed in these cases and may be able to account for the characteristics in the rotor forces mentioned in the previous section.

100% Flow Cases

Table 4.1: Occurences of instability modes for three and four-blade inducers at 100% flow

Three-blade	**Four-blade**	**Instability Mode**
NA	NA	Surge
$\sigma \approx 0.047$	$\sigma \approx 0.041$	Rotating
NA	NA	Alternate Blade

Table 4.1 shows at what cavitation numbers each mode of instability was observed for the two inducer configurations. Both the three-blade and four-blade inducers ran stably at the 100% flow rate with no readily detected instabilities in any of the simulations except for the four-blade case at a cavitation number of $\sigma \approx 0.041$ and the three-blade case at a cavitation number of $\sigma \approx 0.047$. For these two cases, a small amount of rotating cavitation was observed. The rotating cavitation was evident by a unique vapor cavity that formed along one blade and rotated from one blade to the next through time. It is likely this rotating instability is the source for the increased rotor forces calculated for the two cases.

60% Flow Cases

Table 4.2: Occurences of instability modes for three and four-blade inducers at 60% flow

Three-blade	**Four-blade**	**Instability Mode**
$0.010 < \sigma < 0.091$	$0.024 < \sigma < 0.037$	Surge
$0.011 < \sigma < 0.139, \sigma \neq 0.019$	$0.024 < \sigma < 0.037$	Rotating
NA	$0.037 < \sigma < 0.047$	Alternate Blade

Table 4.2 shows at what cavitation numbers each mode of instability was observed for the two inducer configurations. Figure 4.7 illustrates the existence of alternate cavitation on the four-blade inducer. The inception of alternate cavitation occurred at a cavitation number of $\sigma \approx 0.047$ (figure 4.7(b)). At this point, the cavity length to blade spacing ratio (l_s/h) varies between 0.702 and 0.725. As σ decreases (closer to breakdown), the severity of the alternate cavity sizes increase. For example, at a cavitation number of $\sigma \approx 0.045$ (figure 4.7(a)), the cavity length to blade spacing ratio (l_s/h) varies between 0.546 and 0.732.

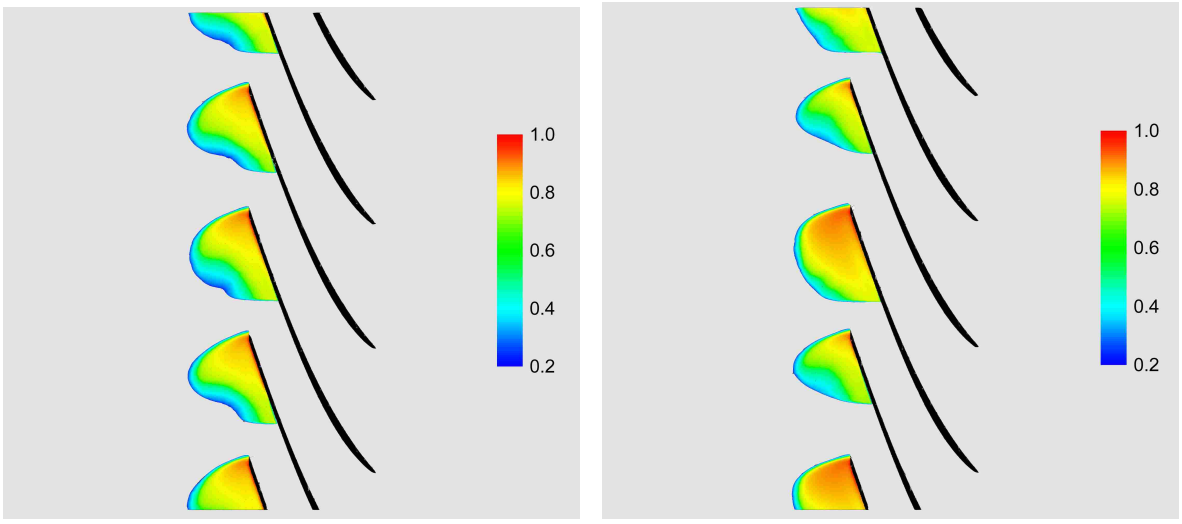

(a) four-blade, 60% flow at $\sigma = 0.047$

(b) four-blade, 60% flow at $\sigma = 0.045$

Figure 4.7: Contour plots of volume fraction of vapor at 98% span on the four-blade inducer at 60% flow.

Figure 4.8 shows the growth and complete collapse of a vapor cavity surging upstream of the impeller for both the three and four-bladed inducers at off-design. This surging cavitation upstream of the inducer has been observed experimentally by the authors, but to our knowledge has not before been captured numerically. The first case where this upstream cavity was observed for the three-blade inducer was at $\sigma \approx 0.038$. Similarly the first time a cavity was observed for the four-blade inducer was at at $\sigma \approx 0.029$. For both cases, the beginning of this upstream surging cavitation correlates with the sudden increase in rotor forces observed in figure 4.6. For the three-blade inducer, rotor forces increased by over 265% between $\sigma \approx 0.091$ and $\sigma \approx 0.038$; and for the four-blade inducer, rotor forces increased by over 385% between $\sigma \approx 0.037$ and $\sigma \approx 0.029$.

The characteristics of this upstream cavity was also quite different between the three and four-bladed inducers. The cavity upstream of the four-blade inducer grew and collapsed symmetrically, whereas the cavity for the three-blade inducer never grew to the same size as the cavity for the four-blade case. It also didn't form symmetrically in the middle of the duct, instead it formed asymmetrically to one side and rotated with the rotor.

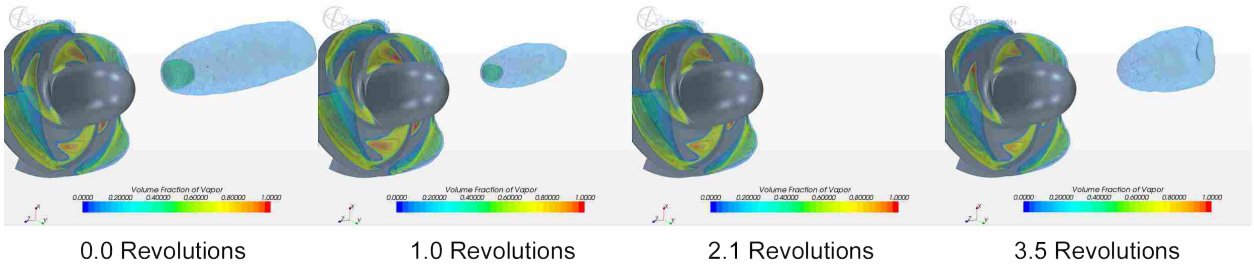

(a) four-blade, $\sigma \approx 0.046$, over a period of 3.5 revolutions

(b) three-blade, $\sigma \approx 0.029$, over a period of 2.1 revolutions

Figure 4.8: Sequence of isometric views over time showing isosurface of vapor fraction greater than 0.1 for the three and four-blade inducers

Figure 4.9 illustrates the motion of the rotating cavitation observed on the three-blade inducer. Through 5.1 revolutions at a cavitation number of $\sigma = 0.0377$ and 0.8 revolutions at a cavitation number of $\sigma = 0.139$, the blade with a smaller cavity length is shown to change from one moment in time to the next. The instability began at a cavitation number of $\sigma \approx 0.139$ where a very small rotating disturbance is present (see figure 4.9(b)). At this point, l_s/h varies between 0.18 and 0.32. As we further approach breakdown the disparity between the large and small cavity lengths along the blades get larger. For example, at a cavitation number of $\sigma \approx 0.038$, l_s/h varies between 0.24 and 0.87. Considering the four-blade inducer doesn't start to see alternate cavitation until $\sigma \approx 0.047$, we believe that this rotating cavitation explains why the three-blade inducer has

higher rotor forces than the four-blade inducer for cavition numbers greater than 0.05. The nature of rotating cavitation ensures that the cavity formation is asymmetric and therefore must also have a circumferentially unbalanced pressure field that correlates to larger rotor forces.

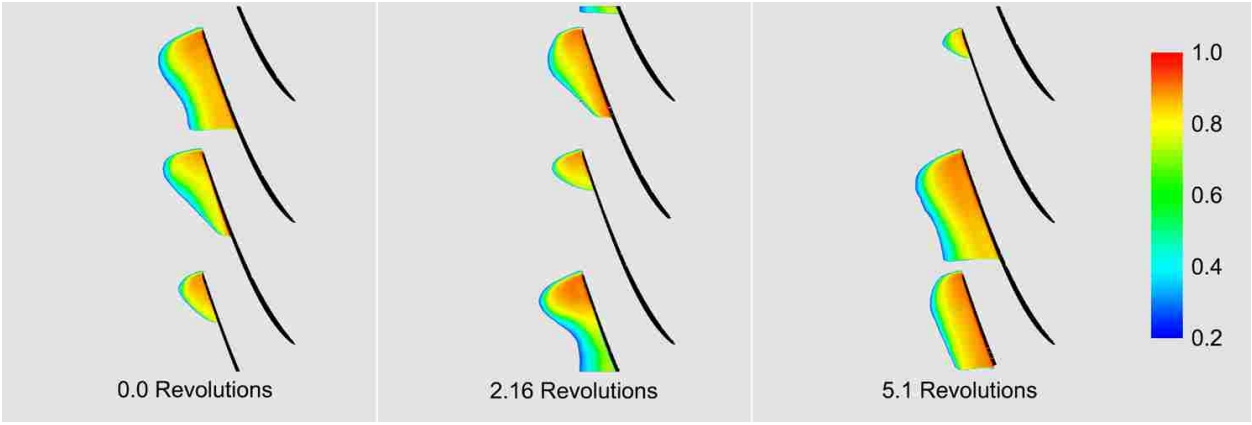

(a) three-blade, $\sigma = 0.0377$, taken over 5.1 revolutions

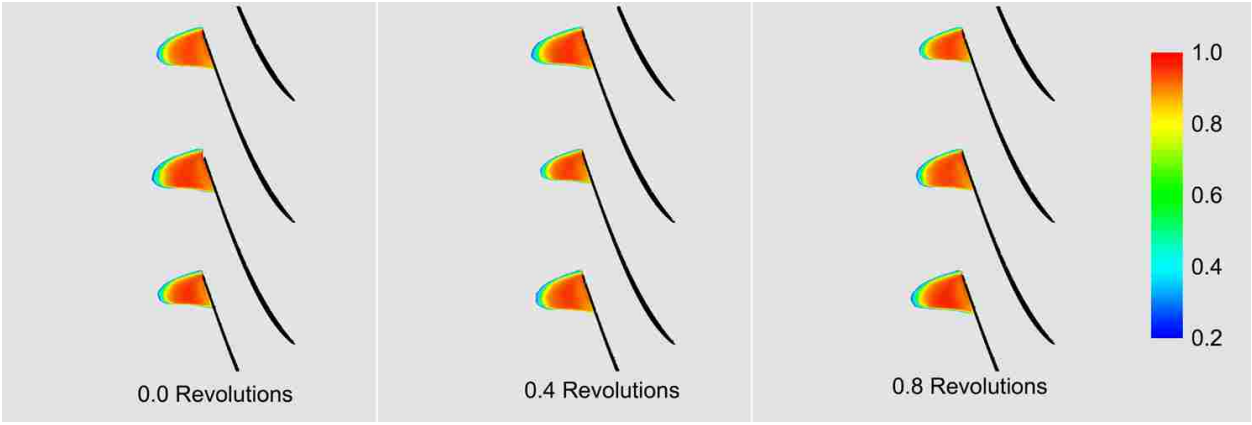

(b) three-blade, $\sigma = 0.139$, taken over 0.8 revolutions

Figure 4.9: Sequence of contour plots of vapor fraction at 98% span over time on three-blade inducer at 60% flow.

There is one other noteworthy instability observed with the three-bladed inducer at 60% flow: at a cavitation number of nominally 0.019, the rotating cavitation stops and turns into a type of cavitation surge along the surface of the blades. Figure 4.10 is a sequence of images showing the growing and shrinking behavior of the cavity. The cavity length to blade spacing ratio (l_s/h) oscillates between 0.728 and 1.028. Because of the uniformity of the vapor cavities, the normalized average rotor force for this cavitation number is significantly lower than for the

cases at neighboring cavitation numbers (only 56.0 as compared to 288.0 for $\sigma = 0.013$ and 528.3 for $\sigma = 0.038$). It's also important to note that because of the surging behavior of the cavity, the inducer experiences large pressure and load spikes which causes the maximum rotor force to be significantly higher (see figure 4.6). This form of cavitation surge is only observed at this cavitation number. At a lower cavitation number, the three-blade inducer returned to exhibiting rotating cavitation.

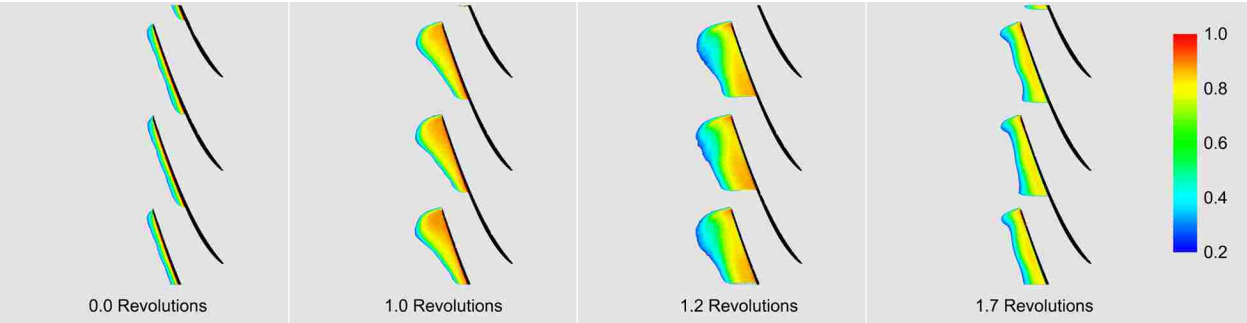

Figure 4.10: Sequence of contour plots of vapor fraction at 98% span for three-blade inducer at $\sigma \approx 0.019$ over a period of 1.7 revolutions

4.7.4 Conclusions

There are several modes of cavitation instability that affect the performance of modern inducers including rotating cavitation, alternate-blade cavitation, cavitation surge, and vortex cavitation. The research compared the cavitation effects of identical three and four-bladed inducers. CFD simulations were run at design flow coefficient and at 60% flow coeffecient with varying inlet pressures in order to analyze the effects of cavitation for both inducer configurations as they go through breakdown.

At design flow rates, there were very small differences between the three and four-blade inducers. Both inducers behaved very stably, except for a minimal appearance of rotating cavitation at a cavitation number of about $\sigma = 0.044$ for both inducers. The largest difference for the on-design cases was the large increase in rotor forces that was nearly three times larger for the three-bladed inducer than for the four-blade.

At off-design flow rates, the differences between the two inducers became much more apparent. Overall, the four-blade had a higher head rise than the three-blade ($\psi_{norm} = 1.42$ compared to $\psi_{norm} = 1.33$). The largest difference, however, was in the forces experienced by the rotor.

For higher cavitation numbers (greater than $\sigma \approx 0.058$), the four-blade had no noticeable instability present, whereas the three-blade had noticeable rotating cavitation for cavitation numbers as high as $\sigma \approx 0.139$. It is most likely due to a combination of the existence of rotating cavitation at these higher cavitation numbers and its asymmetric nature that the three-blade experienced forces that were much higher than those of the four-blade (with normalized maximum forces around 100 for the three-blade compared to around 10 for the four-blade).

For lower cavitation numbers ($\sigma < 0.037$), both the four and three-blade inducers experience a surging vapor cavity upstream of the inducer. The four-blade's upstream cavity was symmetrically balanced in the duct and grew much larger than for the three-blade case. In addition to being smaller than the four-blade's cavity, the three-blade's cavity formed to one side of the duct and rotated with the rotor. It may be because of the larger oscillations with the growth and collapse of the four-blade's cavity that rotor forces for the four-blade increased to match those for the three-blade cases.

Because of the reduced rotor forces, the symmetric formation of cavitation surge and alternate-blade cavitation, and the delayed inception of cavitation instabilities at 60% flow coefficient, the four-bladed inducer configuration was chosen to be used in future phases of this research.

4.8 Acknowledgments

We would like to thank the Fulton Supercomputing Lab for providing the tremendous resources needed for our simulations, CD-adapco for their technical support and training in using their CFD package, and NASA for their financial support with the research for this paper.

CHAPTER 5. AN ANALYSIS OF THE EFFECTS OF INLET BLADE ANGLE ON INDUCERS WITH AND WITHOUT A STABILITY CONTROL DEVICE

5.1 Contributing Authors and Affiliations

Ryan C. Cluff, Ryan K. Lundgreen, Steven E. Gorrell, R. Daniel Maynes
Department of Mechanical Engineering, Brigham Young University, Provo, UT 84602

Kerry Oliphant
Concepts NREC, White River Junction, VT. 05001, USA

5.2 Abstract

Three-dimensional single-phase steady CFD simulations were run on four-blade inducer geometries of 7°, 9°, 11° and 14° inlet tip blade angles with a stability control device (SCD) installed. The simulations were ran at multiple flow coefficients. Results show strong correlations between the inducer efficiency and head rise to the local mass flow gain experienced due to the recirculating flow through the SCD. A best fit curve was generated to predict mass flow gain based on the inducer's inlet tip blade angle and flow coefficient. Based on this research, the ability to predict mass flow gain and consequently efficiency and head rise for similarly designed inducers with varying inlet blade angles has been demonstrated.

[2]This chapter is a manuscript in development for submission. The formatting of the paper has been modified to meet the stylistic requirements of this thesis.

5.3 Nomenclature

$$\phi = \frac{Q}{AU_{tip}}$$
$$\sigma = \frac{P_{01} - P_v}{\frac{1}{2}\rho U_{tip}^2}$$
$$\psi = \frac{P_{08} - P_{00}}{\rho U_{tip}^2}$$
$$\eta = \frac{\dot{m}_{00} * \frac{P_{02} - P_{00}}{\rho}}{T * \Omega}$$
$$NPSH = \left(\frac{P_1}{\rho g} + \frac{V_1^2}{2g}\right) - \frac{\rho_v}{\rho g}$$
$$NSS = \frac{N\sqrt{Q}}{NPSH^{0.75}}$$
$$CorrectedNSS = \frac{NSS}{(1 - (\frac{r_{1h}}{r_{1t}})^2)^{0.5}}$$
$$\alpha = \beta_b - \beta_1$$
$$S = \frac{c}{h}$$

α	Incidence Angle $[deg]$
β_1	Relative Velocity Flow Angle $[deg]$
β_b	Inlet Blade Angle $[deg]$
η	Efficiency $[-]$
μ	Dynamic Viscosity $[m^2/s]$
ρ	Density $[kg/m^3]$
σ	Cavitation Number $[-]$
ϕ	Flow Coefficient $[-]$
ψ	Head Rise Coefficient $[-]$
Ω	Rotational Speed $[rad/s]$
A	Inlet Area $[m^2]$
c	Blade Chord Length $[m]$
g	Gravity $[m/s^2]$

h	Blade Spacing $[m]$
K	Cavitation Compliance $[-]$
M	Mass Flow Gain Factor $[-]$
$\dot{m}$	Mass Flow Rate $[kg/s]$
N	Rotational Speed of Pump$[Rpm]$
$NPSH$	Net Positive Suction Head $[m]$
Nss	Net Suction Specific Speed $[-]$
P	Local Static Pressure $[Pa]$
Q	Volumetric Flow Rate $[m^3/s]$
S	Solidity $[-]$
T	Torque $[n-m]$
U_{tip}	Blade Tip Speed $[m/s]$
V	Local Fluid Velocity $[m/s]$
$\forall$	Volume $[m^3]$

Subscripts, superscripts, and other indicators

$[\,]_0$	indicates [ ] is a property at the inlet of the domain
$[\,]_{0(\,)}$	indicates [ ] is a stagnation property according to the ( ) subscript
$[\,]_1$	indicates [ ] is a property at 2mm upstream of leading edge of inducer
$[\,]_2$	indicates [ ] is a property at 2mm downstream of trailing edge of inducer
$[\,]_8$	indicates [ ] is a property at the outlet of the computational domain
$[\,]_C$	indicates [ ] is of the vapor cavity
$[\,]_{norm}$	indicates [ ] is normalized by the I7no inducer at 100% flow
$[\,]_h$	indicates [ ] is a property at the hub of the rotor blade
$[\,]_t$	indicates [ ] is a property at the tip of the rotor blade
$[\,]_v$	indicates [ ] is a property of the vapor state

5.4 Introduction

In this section, an introduction to the background of inducers and the role they play in an high-speed turbopump will be made. The importance that the incidence angle plays in the performance of the inducer and how it can affect the design of inducers will also be discussed.

5.4.1 Background

A pump's suction performance can be measured by its ability to operate at low inlet pressures. There exist many applications for which high-suction performance pumps are desired. One such application is for the propellant feed system of space launch vehicles. The propellant feed system pumps the fuel from the holding tank to the high pressure chamber injectors. Producing a pump with higher suction performance (having a lower required net positive suction head [NPSH]) allows for lower required propellant tank pressure. This in turn reduces the structural requirements for the tank and ultimately reduces the weight and payload costs for the entire vehicle. Other applications that would benefit from high suction performance pumps include liquefied natural gas transfer pumps and boiler feed pumps. One of the main components that affect the suction performance of the pump is the inlet impeller, also known as the inducer. It has been shown that greater suction performance can be attained, but often at the loss of structural integrity and the ability to operate stably at off-design flow rates [1]. Because of the conflicting nature between designing an inducer with high suction performance and one that can operate stably over a large range of flow rates, finding the ideal balance makes the inducer one of the most difficult components to design properly.

The purpose of the inducer is to provide sufficient pressure rise so as to advert cavitation from occurring in downstream components. Cavitation occurs when a fluid's local pressure drops below its vapor pressure and vapor cavities form, normally along the suction side of the blade, which can lead to debilitating effects on the pump such as:

1. large reduction in head rise when the vapor cavity reaches the size of the inducer's inlet throat

2. blade damage caused by the growth and collapse of cavitation bubbles

3. blade structural failure and inconsistent mass flow rates. This can cause catastrophic changes in engine thrust and is generated by large instabilities due to the interaction between the flow and the vapor cavities.

Figure 5.1 shows the relationship between suction performance and inlet flow coefficient by comparing several cold water tests of various inducers with the Brumfield criterion. The Brumfield criterion is the theoretical maximum suction performance possible at a given flow coefficient, without any thermal suppression head effects (TSH) [4]. As shown in the figure, suction performance is increased as the inlet flow coefficient is reduced. Generally, suction performance can be increased dramatically with small decreases in flow coefficient; however, in practice it is difficult to design an inducer that can operate stably at a flow coefficient below 0.06 [1]. As the flow coefficient decreases, the inlet relative flow angle also decreases. For inducers designed to operate at very low flow coefficients (ϕ), the inlet relative flow angle begins to approach zero. In order to prevent flow separation from the blade, an incidence angle (α) of nominally $+2^\circ$ [2] must be maintained and this is done by designing a similarly low inlet blade angle. Incidence is the angle between the inlet rotor blade and the relative velocity vector (see figure 5.2). Small inlet blade angles results in a decreased inlet throat area which can expose the pump to premature breakdown, since there isn't as much space to absorb the vapor cavities. Breakdown refers to the point where sufficient cavitation has developed such that a small decrease in cavitation number results in a drastic loss of head rise. It is possible to slightly increase the throat area by decreasing the blade thickness; however this is done at the expense of reducing the structural integrity of the rotor. There are other drawbacks to having small inlet blade angles. With small blade angles, small changes in flow coefficient result in large changes of flow incidence which limits the inducer's ability to operate at off-design flow coefficients.

When planning for and designing around modes of cavitation instability, incidence is a key parameter to consider. There exist correlations between unsteady characteristics [16] and vapor length [17] with the parameter $\sigma/2\alpha$ where σ is the cavitation number and α is the incidence angle. Tsujimoto et al. [9] further showed that unsteady modes of cavitation (such as the formation of rotating cavitation and cavitation surge) begin developing when the cavity length reaches about 65% blade spacing (distance between blades). Higher incidence promotes flow separation from

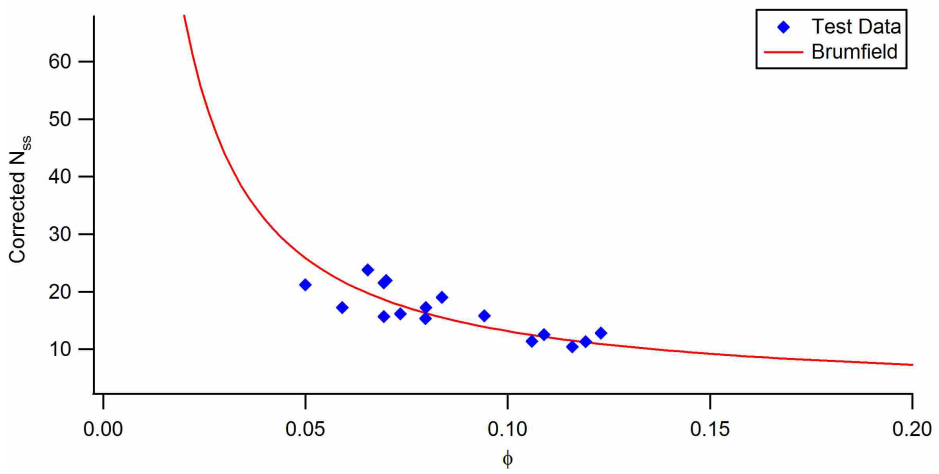

Figure 5.1: Corrected N_{ss} as a function of flow coefficient for various cold water inducer tests compared to Brumfield criterion [1]

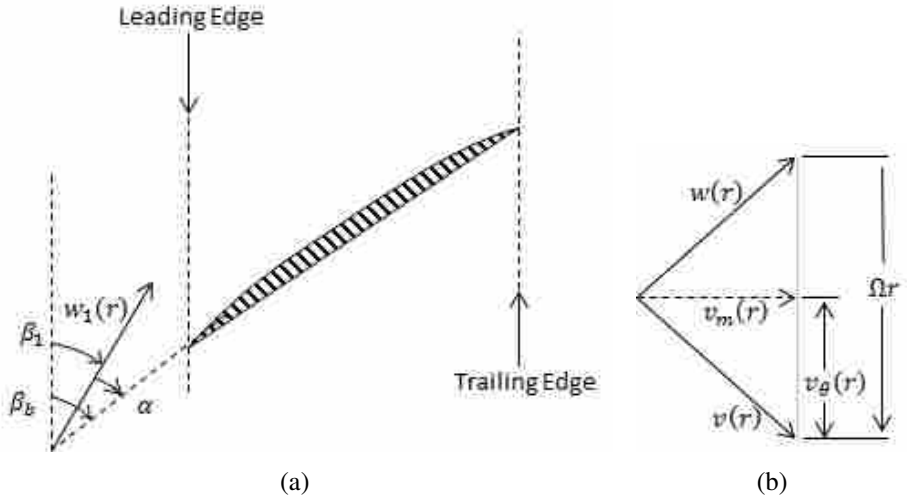

Figure 5.2: Showing the definitions of incidence angle $\alpha(r)$, velocity $v(r)$, meridional velocity $v_m(r)$, angular velocity $v_\theta(r)$, relative velocity $w(r)$, and blade velocity Ωr

the suction side of the blade. This flow separation further reduces the fluid's static pressure and encourages cavitation development.

It is not optimal, however, to design an inducer that operates with a zero-degree incidence. In order to ensure that cavitation occurs on only the suction surface of the blade, it's preferable to design for an incidence of nominally $+2^\circ$ [2]. Any higher incidence can result in premature cavitation development and premature breakdown.

The stability control device, or SCD, was designed by Concepts NREC to permit an inducer to operate at lower flow coefficients without requiring small blade angles. The SCD includes a recirculation duct that creates a localized increase in flow throughout the initial portions of the inducer (see figure 5.3). Krise [3] studied the effects of a SCD on a flat-plate inducer. The same inducer at the same operating conditions were compared with one having the SCD installed and the other without. Figure 5.4 shows the velocity contours of a longitudinal cross-section of both simulations. It was observed that the significant backflow present at the tip of the leading edge for the inducer without the SCD was successfully removed for the inducer with the SCD. Additionally, it was shown that with the SCD installed, cavitation inception was delayed and the flat-plate inducer was able to function at operating conditions well beyond the limits of the inducer without the SCD, due to its ability to locally increase the flow coefficient to that at which the inducer can successfully operate. It also showed an overall stabilizing effect to the flow, especially when operating at off-design flow rates.

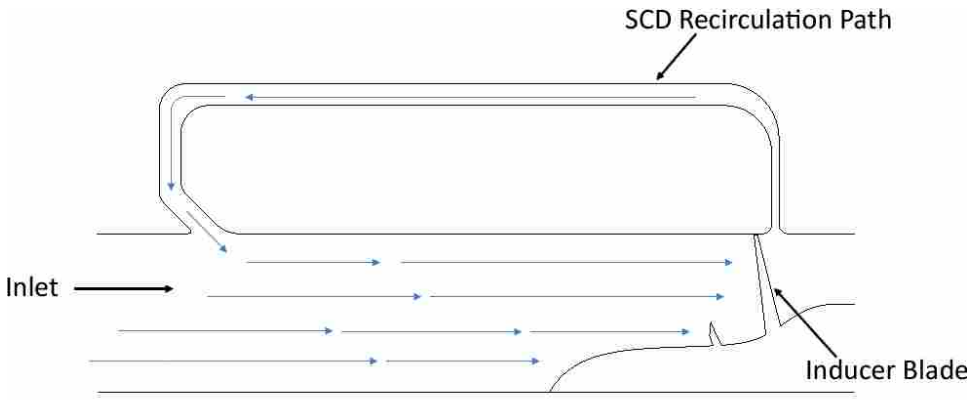

Figure 5.3: Diagram of Stability Control Device.

5.4.2 Objectives

Significant work has been made in assisting in the design process for a standard inducer. Given certain requirements such as NPSH, range of operating flow coefficients, and blade angle, it is a fairly straightforward process to create an inducer design as well as have reasonable expectations of performance and stability. Designing for an inducer with a SCD is not as straight forward.

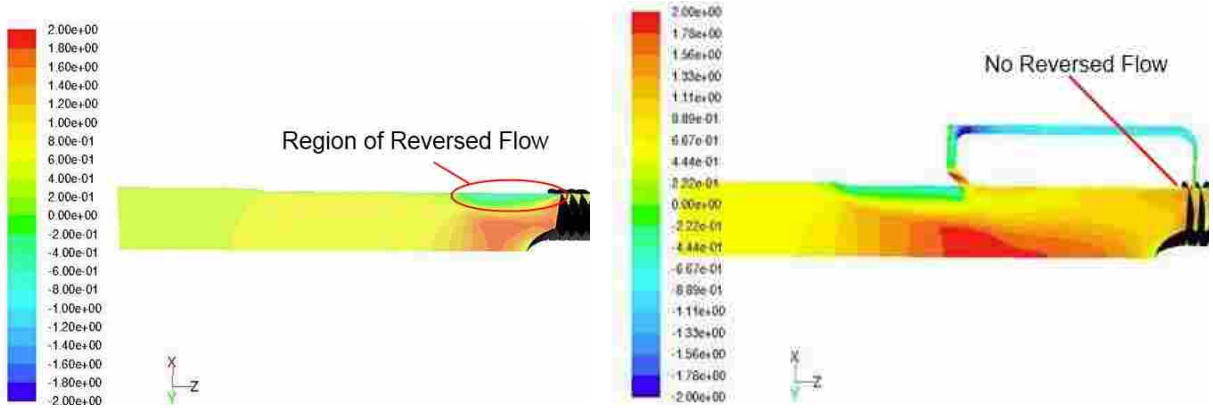

(a) Without SCD (b) With SCD

Figure 5.4: Velocity contours of 5.4(a) without the SCD and 5.4(b) with the SCD [3]

It is the goal of this research to continue building a knowledge base for inducers with a SCD. This will be done by analyzing how certain flow characteristics, such as incidence angle and head rise, change once a SCD is introduced. For the first time in open literature incidence as a function of blade span will be compared between the same inducer with and without a SCD. This will provide insight as to why the use of a SCD drastically changes the flow characterstics within the recirculation region of the inducer. Additionally, work will be made to develop methods for predicting major pump performance metrics (such as head rise, incidence, and efficiency) for inducers that use a SCD, based on pump design.

5.5 Methodology

In this section, the methods used for design variables, grid generation, creating boundary conditions, and determining grid independence and convergence will be discussed.

5.6 Design Variables

This research involves comparing the performance of inducers with varying geometry configurations. In order to make the comparison several design variables will be used. These include head coefficient (ψ), efficiency (η), and mass flow gain ($\dot{m}_{gain}$). These design variables are defined in equations 5.1 thru 5.3 respectively.

$$\psi = \frac{P_{08} - P_{00}}{\rho U^2} \tag{5.1}$$

Head coefficient (ψ) is defined in equation **??** where P_{08} the total pressure of the outlet of the domain, P_{00} is the inlet total pressure, and ρ is the density of the liquid. For this application, water was the working fluid with a density of $\rho = 998.2^{kg}/_{m^3}$. P_{08} and P_{00} were calculated at the outlet and inlet geometry surfaces respectively. For reference of these surfaces, see figure 5.5. And finally, U_{tip} was calculated as the maximum velocity on the rotor. The head coefficient is used to measure the non-dimensional head rise of the pump and is used widely in the turbomachinery industry. In this research a normalized head coefficient may be used. Unless otherwise specified, the normalized head coefficient is defined as the head coefficient divided by the head coefficient of the baseline geometry at 100% flow (I7no inducer at $\phi = 0.07$). The purpose of the normalized head coefficient is to be able to compare performance between the inducers on a relative basis.

$$\begin{aligned} \eta &= \frac{w_{ideal}}{w_{actual}} \\ &= \frac{\dot{m}_{00} * \frac{P_{02} - P_{00}}{\rho}}{T * \Omega} \end{aligned} \tag{5.2}$$

Efficiency (η) is defined in equation 5.2 where w_{ideal} is the ideal work input to the machine and w_{actual} is the actual work input to the machine. $\dot{m}_{00}$ is the mass flux at the inlet and P_{02} is the total pressures at the trailing edge of the inducer. T is the torque calculated on the rotor and Ω is the angular velocity of the rotor, which in this research is a constant 628.3 $^{rad}/_{s}$. Efficiency is a measure of how well the machine is able to convert the input (torque) into the desired output (head rise).

$$\dot{m}_{gain} = \frac{\dot{m}_{01}}{\dot{m}_{00}} \tag{5.3}$$

Mass flow gain ($\dot{m}_{gain}$) is defined in equation 5.3 where $\dot{m}_{01}$ is the local mass flow at the inducer leading edge and $\dot{m}_{00}$ is the local mass flow at the inlet. Mass flow gain provides insight

to how much recirculation occurs through the SCD. As part of this research, it will be shown how mass flow gain is linked with the other design variables (head rise and efficiency).

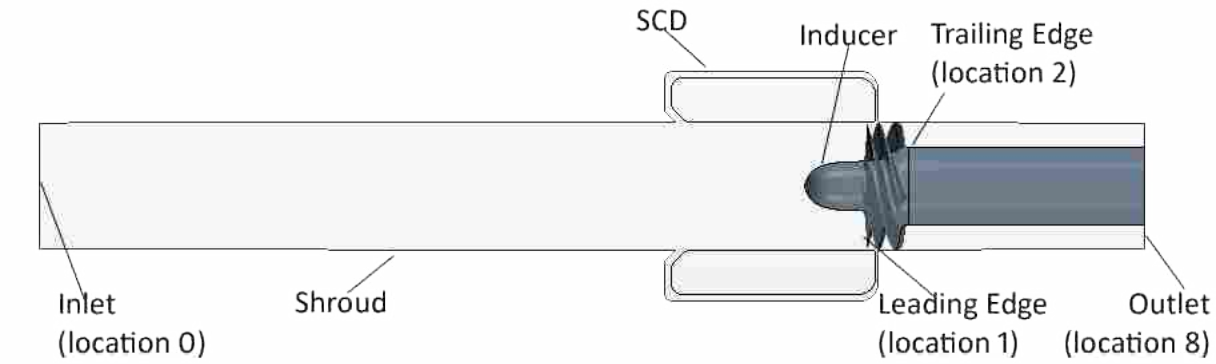

Figure 5.5: Side view of I7 geometry

5.6.1 Geometry

This study investigates the performance of multiple inducer geometries. All geometries were derived by a "baseline" geometry which had a tip blade angle of 7°, tip solidity of $S = 2.09$, and a design point flow coefficient of $\phi = 0.07$. This baseline geometry is referred to as "I7". Table 5.1 lists all the configurations along with their inlet tip blade angle and any additional unique information. All geometries shared the same solidity except for the I14s inducer which was created to have the same axial length as the I7 configuration, resulting in a much lower solidity. Additionally, all inducers were coupled with the same SCD geometry except for the I7opt, whose SCD was intended to improve the mass flow gain through the inducer regardless of the net mass flow rate. The I7opt's SCD inlet throat was 55% wider and its outlet location was 20% further upstream than the standard SCD. The scope of this research does not include altered SCD geometries, however the I7opt was included in order to demonstrate how inducer results may change with altered SCD geometries. The majority of the analysis presented here was limited to geometries with the same SCD.

Table 5.1: Geometry Information

Name	Inlet Tip Blade Angle	Description
I7	7°	Baseline Geometry
I7opt	7°	I7 with optimized SCD
I7no	7°	I7 without SCD
I9	9°	Same Solidity as I7
I11	11°	Same Solidity as I7
I14	14°	Same Solidity as I7
I14s	14°	Same Axial Length as I7

5.6.2 CFD Simulation

CD-adapco's STAR-CCM+ v7 was the solver used in this study. In order to analyze flow characteristics without the presence of cavitation, simulations were run in a single-phase steady environment. Water with a constant density of 998.2 $^{kg}/_{m^3}$ was used as the working fluid. Turbulence effects were estimated using the Realizable k-ε two-layer model. The two-layer approach allows the k-ε model to be applied to the viscous sublayer. In this approach, the computation is divided into two layers. The near-wall layer's turbulent dissipation rate ε and turbulent viscosity μ are specified as functions of the wall distance and are blended with the values computed from solving the transport equation far from the wall. The velocity and pressure flow equations were solved using STAR-CCM+'s Segregated Flow solver which solves them in an uncoupled manner and updates the flow field using a SIMPLE-type algorithm. The solver accuracy was 2^{nd} order in space and 1^{st} order in time.

Grid Generation

A mesh of the domain was created using STAR-CCM+'s meshing tool. The geometries were first created on a CAD package and imported to STAR-CCM+ in the STP format. STAR-CCM+'s polyhedral and prism-layer meshing models were employed. The polyhedral mesher generated polyhedral cells throughout the domain. The prism-layer mesher created 3 prism layers near the surface boundaries in order to improve the accuracy of the boundary-layer approximations. Cell count ranged from 6.5 million to 10 million cells depending on the inducer geometry. In order to better resolve the physics near the high-gradient regions, a finer grid was necessary for the

region near the inducer blades and SCD. A conical volumetric control (Figure 5.6) was created to refine the mesh in the region near the inducer blades. Within this region, the target cell size was reduced by 75% and the number of prism layers was increased from 3 to 10 layers. Another volumetric control, annular in shape, was created to refine the mesh near the SCD passage. In this region, the number of prism layers was increased from 3 to 5 and the target cell size was reduced by 70%. The increased resolution resulted in an acceptable maximum Wall y^+ value of 70 and an average Wall y^+ value of 17. Low y^+ values allow for a wall-treatment that assumes the viscous sublayer is properly resolved [15]. High y^+ values (above 100) rely on a wall-function approach that approximates the viscous sublayer effects and assumes the near-wall cell lies within the logarithmic region of the boundary layer. Y^+ values between 10 and 100 require a type of hybrid function that is able to merge both wall treatments. STAR-CCM+'s all-$Y+$ wall treatment, which was employed in these cases, is an example of such a hybrid function. This wall treatment attempts to emulate the high y^+ wall treatment for coarse meshes and the low y^+ treatment for fine meshes.

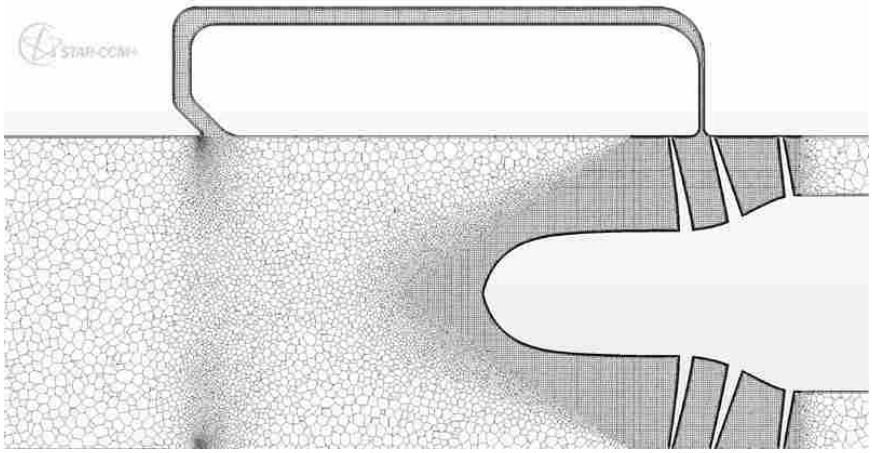

Figure 5.6: Cross section showing mesh generated for I9 inducer. Conical volumetric control allows for refined mesh near inducer blades.

Boundary Conditions

The domain was specified as a rotating relative reference frame at 6,000 rpm. The shroud and rotor were set as no-slip boundary walls with the rotor fixed to the rotating reference frame

and the shroud fixed to be stationary to the absolute reference frame. The inlet boundary was set as a mass-flow inlet, where the mass flux normal to the inlet surface may be controlled. The outlet boundary was set as a radial-equilibrium pressure outlet, where the pressure at the hub may be controlled.

Grid Independence

To determine grid independence, two meshes were generated for a slightly different four-bladed geometry. The coarser of the two contained 6,667,204 cells and the finer mesh contained 12,199,553 cells. A critical parameter in determining pump performance is the head coefficient, ψ. Both simulations were run to convergence and their head coefficients averaged over 10 rotor revolutions. With a difference of approximately 0.34%, it was determined that the coarser of the two meshes was adequate.

5.6.3 Time Independence

A time study was conducted on the four-bladed geometry. Time step was varied between $1 \times 10^{-4} s$ (equivalent to 3.6 $^{deg}/_{step}$) and $2 \times 10^{-6} s$ (equivalent to 0.072 $^{deg}/_{step}$). After running each test to convergence, a comparison was made on the head coefficient, efficiency, rotordynamic forces, mass flow gain, and conservation of mass (sum of mass flux between inlet and outlet, this should be 0) performance monitors. It was determined that a time step of 1.39×10^{-5} (equivalent to 1 $^{deg}/_{step}$) was adequate for the research. At this time step, the performance monitors were within 1% of the more refined time step and had a conservation of mass error less than 0.1%.

Convergence

Convergence was determined in a case by case basis based on the following criteria:

1. Residuals were showing a stable behavior. Stable behavior is characterized by normalized residuals dropping generally below 0.1 and levels remaining unchanged for at least $2,000$ iterations (generally simulations were run beyond that point).

2. Monitors for the domain's inlet pressure (P_0), the inducer's exit pressure (P_2), the rotor's torque, and the domain's volume fraction of vapor were flat and unchanging for at least $2,000$ iterations (generally simulations were run beyond that point).

5.7 Results

In this section, the results of the analysis will be presented in three parts: how performance varied across inducer designs, how incidence changed across inducer design and with or without a SCD attached, and correlations that were discovered between mass flow gain, efficiency, and head rise.

5.7.1 Performance

Figure 5.7 shows the head rise normalized by I7no head rise at design as a function of flow coefficient. As would be expected, an increasing head rise with decreasing flow coefficient as well as increasing head rise with increasing blade angle can be seen. There are two exceptions to the latter trend: the I14s inducer had the lowest head rise of all inducers and the I11 is either equal to or had a slightly higher head rise than I14. The I14s inducer was the same as the I14 inducer, except it had a much shorter axial length which resulted in a lower solidity than I14. The I14s axial length was equal to that of the I7 inducer. Because of its shorter length and lower solidity, it is suspected that the I14s wasn't able to transfer as much work into the flow, resulting in an average of 14% lower efficiency than I14 and less of a head rise. The I11 inducer was designed differently than the other inducers. The I11 was designed to optimize throat area throughout the blade passages, and actually performed much more similar to the I14 inducer. As shown later, the I11 and I14 shared nearly identical mass flow gain which may be why their head rise was also similar. It's especially interesting to note that the I7 had a significantly higher head rise than the I7no for all flow coefficients. The only difference between the two inducers is that the I7 has a SCD and the I7no does not. Some preliminary research suggests that one benefit of the SCD is a higher efficiency for the rotor region downstream of the SCD inlet, but that is beyond the scope of this paper.

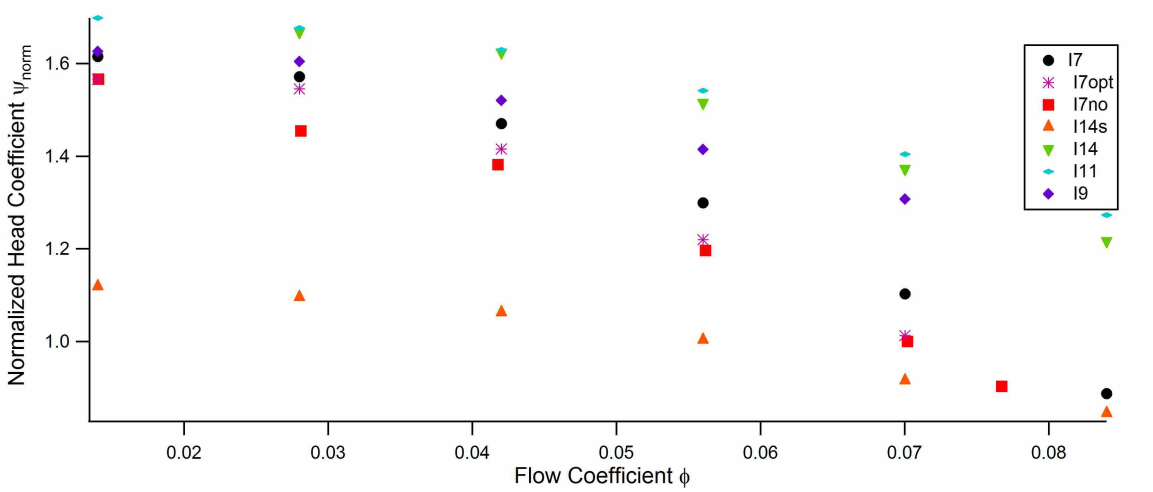

Figure 5.7: Head rise as a function of flow coefficient

5.7.2 Incidence

Figure 5.8(a) shows flow coefficient as a function of tip incidence (95% span). There was a clear distinction between trends for the inducers with and without a SCD. The I7no inducer showed the expected increasing incidence with decreasing flow coefficient. Although not visible with the steady single-phase simulations, the high-incidence levels would normally cause large cavitation growth and instabilities to develop at lower cavitation numbers, as shown in Chapter 4. Over the range of flow coefficients, the inducers with a SCD experienced an incidence change of about 2.2°. Over the same range of flow coefficients, the inducer without a SCD (I7no) experienced an incidence change of 22.6°. This demonstrates a potential benefit from the SCD. Suppressing incidence will reduce the development of instabilities that traditionally limit the minimum flow coefficient at which the inducer may operate. Further research is needed to determine the new limits for an inducer with a SCD.

It is interesting to not only look at the tip incidence behavior, but also the average incidence. Figure 5.8(b) shows flow coefficient as a function of the area-averaged incidence. All of the cases, with the exception of the I7no inducer, showed a general decreasing averaged incidence with decreasing flow coefficient. This goes contrary to the classical expectations of the relationship between incidence and flow rate. Normally, it is expected to have large increases in incidence with decreasing flow rates - which is clearly shown for the I7no inducer in figure 5.8(b).Why the use of the SCD prevents incidence growth and actually reduces the average incidence can be understood

by looking at figure 5.9 which shows axial velocity from hub to tip for both the I7no and I7 inducers at a flow coefficient of $\phi = 0.028$. The case at a flow coefficient of $\phi = 0.028$ was chosen for this example, although the same shape and characteristics are shared for all flow coefficients. Without the SCD, much more reverse flow occurred starting at the blade tip and extending down to about 87% span. Negative axial velocity created a negative flow angle which resulted in larger incidence angles. Conversely with the use of a SCD, instead of a region of reverse flow, the fluid recirculating from the SCD formed a region of higher axial velocity between 70-99% span. This higher-velocity region caused the average incidence to decrease. Additionally, as the net mass flow decreased the amount of recirculating fluid grew and resulted in a larger and more extreme region of higher velocity. This explains the decreasing average incidence with decreasing mass flow rate.

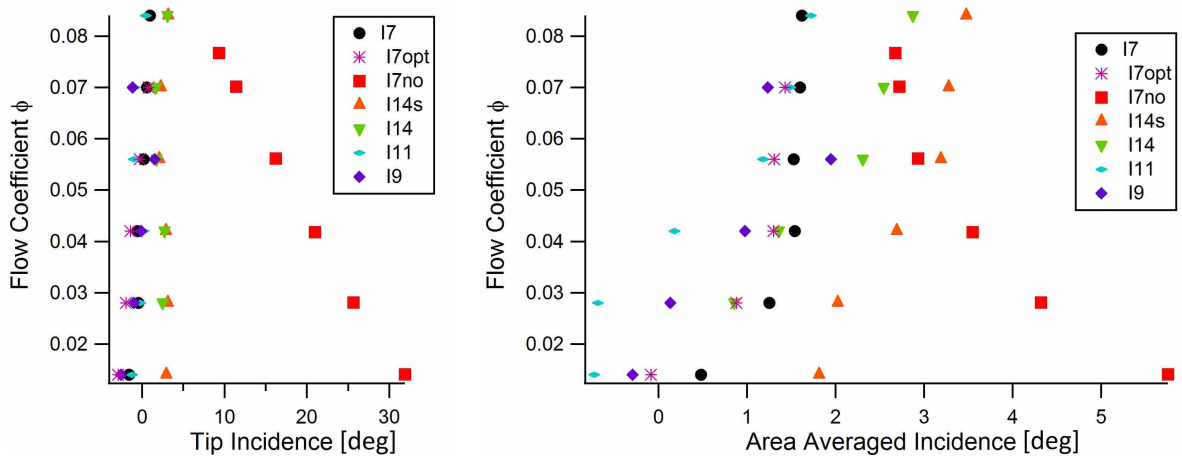

(a) Tip Incidence (95% span)

(b) Area Averaged Incidence

Figure 5.8: Flow coefficient as a function of Tip Incidence 5.8(a) and Area Averaged Incidence 5.8(b) for all inducers.

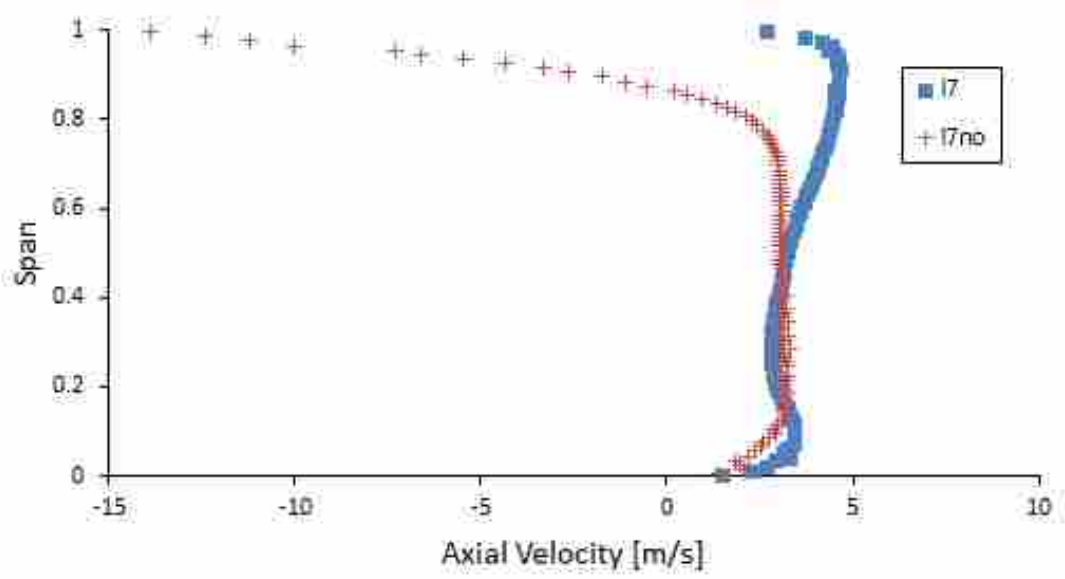

Figure 5.9: Axial Velocity profiles for the I7no and I7 inducers at a flow coefficient of $\phi = 0.028$

5.7.3 Correlations

One objective of this research was to identify correlations to predict performance parameters for inducers with a SCD. The ability to predict an inducer's performance will enable a designer to match an SCD with an inducer.

After a robust data analysis, it was discovered that strong correlations exist between the local mass flow gain and performance parameters generally used to define inducer performance, specifically head rise and efficiency. Mass flow gain is a useful way to measure the impact of the SCD's influence. Higher mass flow gains signify that there is much more recirculation going through the SCD. Figure 5.10 shows the plots of mass flow gain as a function of flow coefficient for each configuration. It was observed that for each inducer geometry mass flow gain decreased with increasing flow coefficient. Additionally, the mass flow gain curve shifted up with increasing inlet blade angle. For example, I7 started with a mass flow gain of about 6 at $\phi \approx 0.01$ and fell to about 1.5 at $\phi \approx 0.07$ while I9 started at a mass flow gain of about 7 and fell to about 2 for the same flow coefficients. Based on the regressions' R^2 value, it was determined that a curve in the form of $A\phi^{-B}$ was a good fit of the data. Figure 5.10 also shows the correlation curve calculated for each geometry. The next step involved combining the equations into one that could be used based on a common parameter.

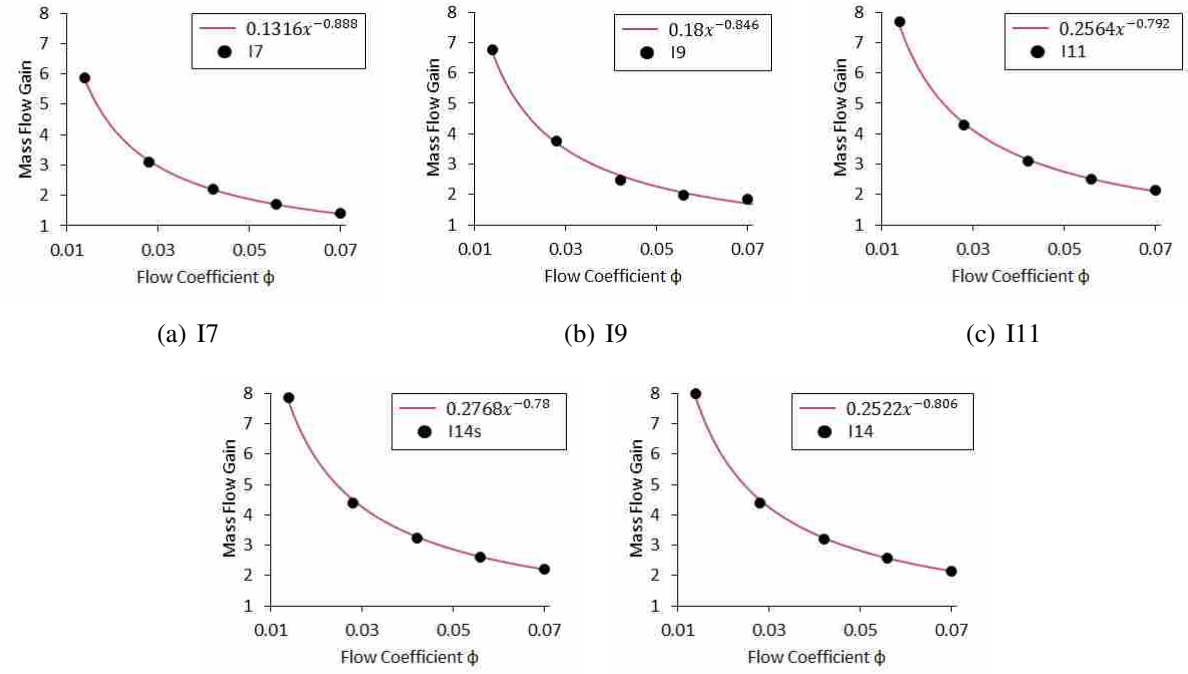

(a) I7 (b) I9 (c) I11

(d) I14s (e) I14

Figure 5.10: Mass flow gain as a function of flow coefficient for the SCD inducers. Symbols are simulation results. Red line is correlation curve.

Figure 5.11 plots coefficients A and B as a function of inlet tip blade angle. A curve fit in the form of $C\beta^{-D}$ was generated for each coefficient. Substituting these equations for their respective coefficients gave a general equation for mass flow gain as a function of flow coefficient and inlet blade angle (equation 5.4). Note at a blade angle of 14 degrees, coefficients A and B have two distinct values. This comes because there were two inducers with a blade angle of 14 degrees: I14 and I14s. Because the only difference between I14 and I14s was the solidity, solidity may be a key parameter to consider when correlating mass flow gain from inlet tip blade angle. In other words, in order to predict mass flow gain strictly from inlet tip blade angle, it's necessary to look at inducers with the same solidity.

$$\begin{aligned} \dot{m}_{gain} &= A\phi^{-B} \\ &= (0.02\beta^{0.9976})\phi^{(1.21\beta^{-0.164})} \end{aligned} \tag{5.4}$$

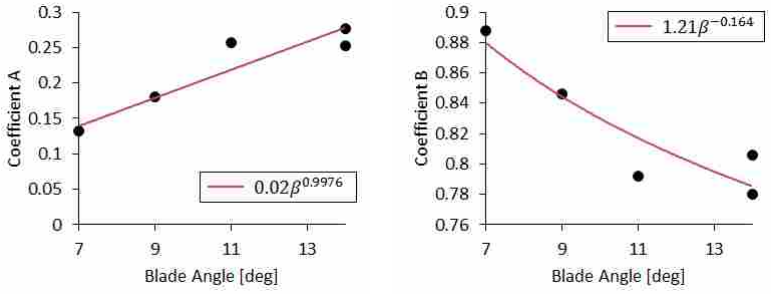

(a) Coefficient A (b) Coefficient B

Figure 5.11: Values for coefficients A and B as a function of inlet blade angle β. The least square regression line is also shown.

To judge how well equation 5.4 predicts the mass flow gain of the inducers, figure 5.12 was generated which plots the error of the predicted mass flow gain as a function of flow coefficient. The error was calculated as

$$error = \frac{\dot{m}_{gain,predicted} - \dot{m}_{gain}}{\dot{m}_{gain}} \tag{5.5}$$

The majority of the error was below $\pm$ 6% and a few errors up to 10%. The distribution of the error consisted of most of the inducers having positive error and the I11 inducer having higher negative error. All of the inducer configurations seem to fluctuate error in a sort of wave shape. The I9 had the most extreme fluctuation in error ranging from +5% to -7%. The error for the I7opt began very negative at -7% and steadily increased with increasing flow coefficient to an error of 4% at the highest flow coefficient. This may be due to the improved SCD that allows for greater recirculation. Particularly at low flow coefficients, this would cause the mass flow gain to be higher than normally predicted (resulting in a negative error). Then as the flow coefficient increases, the benefits of the optimized SCD become less important. Also interesting to note is the I11 error had the highest error magnitude and all of the error was negative. This is likely due to the fact that the I11 has a slightly adjusted blade shape that increases the throat area. As such, it's possible that the I11's larger throat requires more recirculation than the other inducers, and therefore has a consistently negative error. This is demonstrated numerically by the fact that the I11 data point for coefficient A (figure 5.11) is higher than the trendline. This results in the predicted mass flow gain being lower than actual.

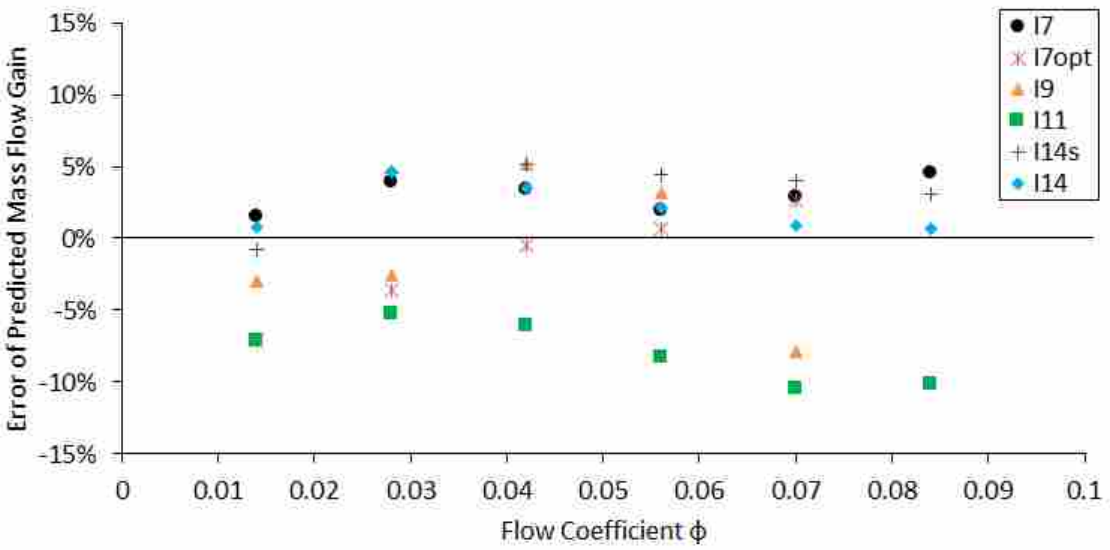

Figure 5.12: Plot of error from predicted mass flow gain using correlation equation

A correlation between head rise and the local mass flow gain was identified. Using a power law relation, equation 5.6 represents the best fit curve for all the inducers except I7no and I14s and gives an estimate to the normalized head rise as a function of mass flow gain. Figure 5.13 plots normalized head rise as a function of mass flow gain for all the inducers and equation 5.6. Equation 5.6 fits the data extremely well for most of the inducers and shows why the data from I7no and I14s was not included. I7no didn't have a SCD, so clearly there wouldn't be any correlation between local mass flow gain and head rise. Also, I14s had a much shorter solidity, so although it was generating the same mass flow gain as the I14, it wouldn't be expected to produce the same head rise.

$$\psi_{norm} = 1.6593 - 3.9565^{-1.2729\dot{m}_{gain}} \tag{5.6}$$

An interesting conclusion from this figure can be drawn. Equation 5.6 flattens out for mass flow gains above 5. Significant improvements in head rise with increasing mass flow gain would therefore not be expected. It is interesting to note that for the I11 inducer, which had an inlet blade angle of 11°, the mass flow gain was already over 2.1 for the 100% case ($\phi = 0.07$). At this point, its normalized head rise was 1.40 which was already 83% of the maximum recorded in figure 5.13. It would be expected then, that inducers with higher blade angles (such as 14° or more), and

therefore higher mass flow gains, to not experience significantly higher normalized head rise. As such, there doesn't appear to be evidence, at least in terms of head rise, to support the need for the inlet blade angle to be any larger than those used in this study (which was 14°).

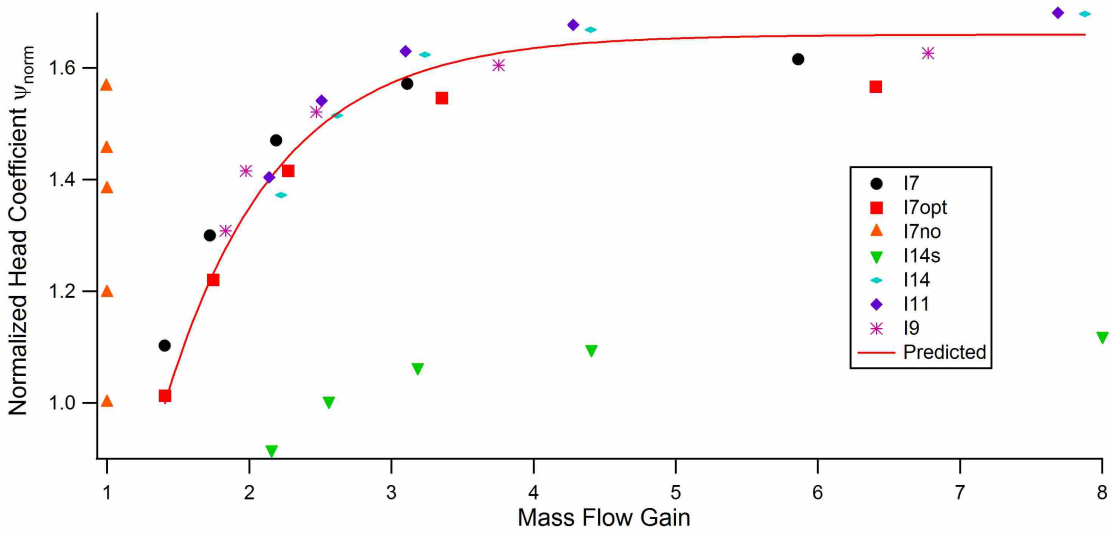

Figure 5.13: Normalized head rise as a function of mass flow gain for all inducers

There is a similar relationship between mass flow gain and efficiency. Using a power law relation, equation 5.7 is the best fit curve to that relationship for all inducers except I7no. Figure 5.14 plots efficiency as a function of mass flow gain as well as equation 5.7. Figure 5.14 shows that efficiency decreased with increasing mass flow gain. This may be due to the fact that higher levels of mass flow gain meant that more fluid was being recirculated through the pump which required work that negatively affected efficiency. Notice how in this plot, I7no was the only inducer that didn't appear to be accurately represented by the predicted curve; unlike equation 5.6 with which both I7no and I14s were not accurately predicted. It would seem then that solidity, which was the only distinguishing difference for the I14s, does not affect efficiency.

$$10.661 + 127.33^{-0.4312\dot{m}_{gain}} \tag{5.7}$$

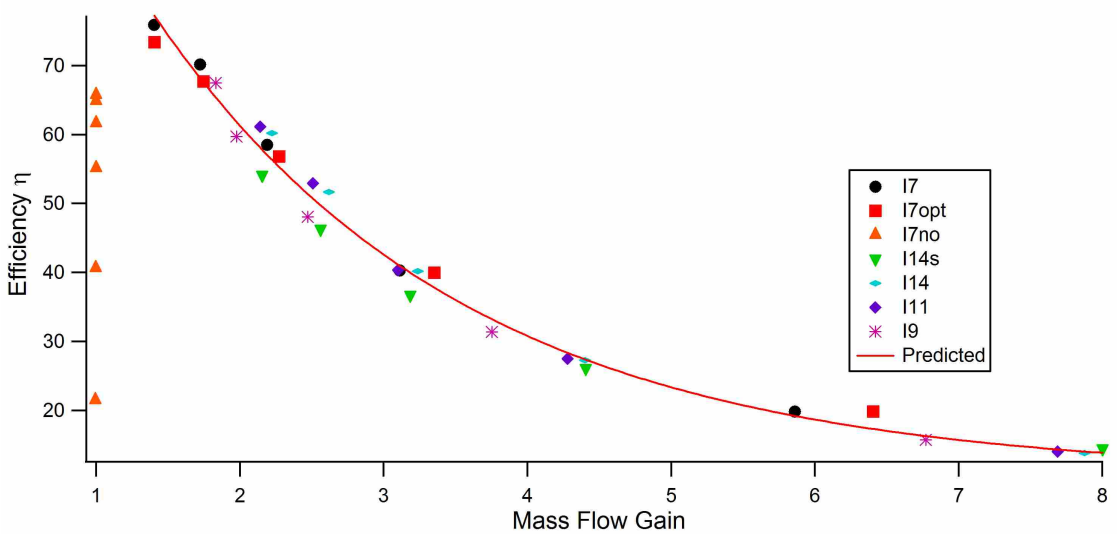

Figure 5.14: Efficiency as a function of mass flow gain for all inducers

Finally, figure 5.15 shows the error plots for the predicted efficiency(figure 5.15(a)) and normalized head coefficient (figure 5.15(b)). In order to prevent a misleading scale, the error for I7no was not included. For both efficiency and normalized head coefficient, nearly all the data laid within 10% of the predicted values. The distribution of error of predicted efficiency appeared to be evenly distributed across all flow coefficients. The distribution of error of predicted head rise is nearly 0 for $\phi < 0.05$ and increases to about 10% for $\phi > 0.05$. The head rise error for I14s hovered around 50% for most flow coefficients, for this reason it was not included in figure 5.15(b). This didn't come as a surprise because, as discussed earlier, its lower solidity resulted in a lower head rise than the other configurations.

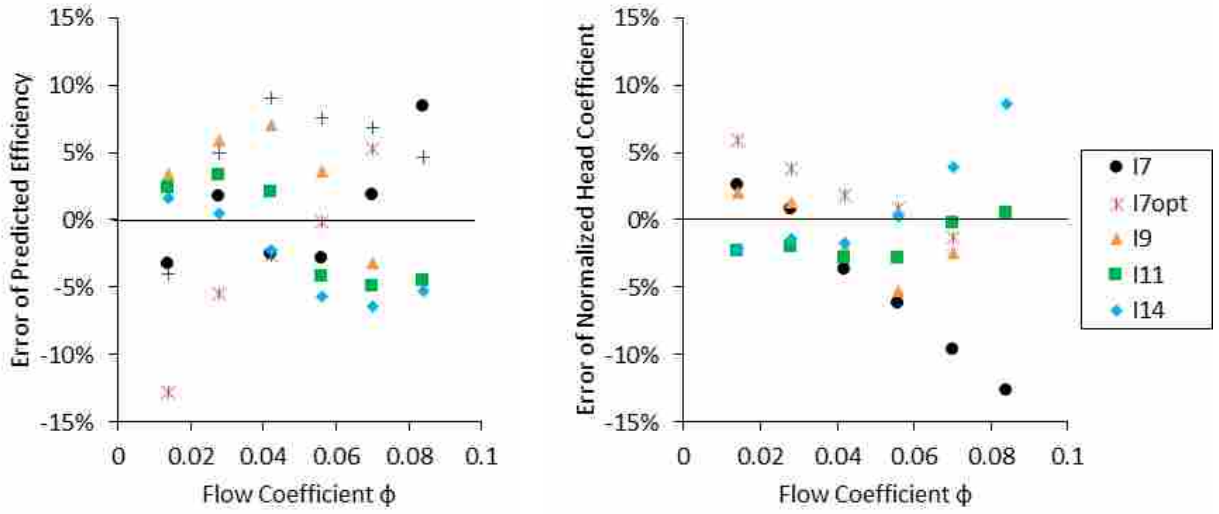

(a) Efficiency

(b) Normalized Head Coefficient

Figure 5.15: Plot of error from predicted efficiency (5.15(a)) and normalized head rise (5.15(b)) using their correlation equations, as a function of flow coefficient

5.8 Conclusions

This paper has begun the work of analyzing non-cavitating flow characteristics for inducers with varying blade angles with a SCD attached. The presence of the SCD introduces recirculating flow that creates a locally increased mass flow rate through a portion of the inducer. It was shown in this paper that an inducer with a SCD attached experiences a higher head rise than an identical inducer without a SCD at design and off-design flow coefficients.

It was also shown in this paper that the increased mass flow generated by the SCD helped to significantly reduce blade tip incidence when operating at off-design flow coefficients, compared to identical inducers without a SCD. At the lowest flow coefficient of $\phi = 0.014$, The I7no (no SCD) had a tip incidence angle of 31.9° compared to the I7 incidence of -1.6°. Further research showed that specifically for the I7no (no SCD) at a flow coefficient of $\phi = 0.028$, reverse flow was observed starting at about 87% blade span. In contrast, no reverse flow was observed for the I7 at any point along the blade. In fact, the recirculating flow through the SCD increased the axial velocity starting at a blade span of about 70%. The increased axial velocity for blade span greater than 70% caused the incidence angle to decrease in that region. This may imply that the inducer's

blade profile needs to be adjusted in order to accommodate the increased velocity caused by the recirculating flow and prevent the negative incidences from occurring.

Mass flow gain provides insight to the extent of influence that the SCD has on the flow. Mass flow gain has strong correlations with head rise and efficiency. It was shown that it is possible to predict the level of mass flow gain from the inlet blade tip angle for inducers with varying inlet blade angles. With the equations presented in this research, it was possible to predict the mass flow gain with a mean average percent error of 2.8%. Mass flow gain was shown to increase with increasing blade angles and decreasing flow coefficient.

One objective of this research was to identify correlations to predict performance parameters for inducers with a SCD. This paper presented correlations between efficiency and head rise with mass flow gain for inducers with a SCD. With the equations presented in this research, it was possible to predict head rise and efficiency for the inducers used in this study with a mean average percent error of 5.0% and 4.4% respectively. Head coefficient increases with mass flow gain, but levels out at a flow coefficient of about 3.7. This may imply that designing an inducer with a mass flow gain greater than 3.7 doesn't have any advantage in regards to head rise. Efficiency displayed a negative relationship with increasing mass flow gain. It was also shown that the accuracy of these equations require that the inducers share at least the same solidity. Future work will need to further investigate how other distinguishing physical characteristics (such as SCD passage and blade shape) can affect these relationships.

5.9 Acknowledgments

We would like to thank the Fulton Supercomputing Lab for providing the tremendous resources needed for the simulations, CD-adapco for their technical support and training in using their CFD package, and NASA for their financial support with the research for this paper.

CHAPTER 6. CONCLUSIONS AND RECOMMENDATIONS

6.1 Conclusions

There exist many applications where a pump with very high suction performance can be very advantageous. An inducer is fundamental in designing high suction performance pumps. Preliminary work performed by Krise [3] laid the groundwork for this research. It was shown that with a SCD, cavitation inception was delayed. It also showed an overall stabilizing effect to the flow, especially when operating at off-design flow rates. It was the goal of this research to continue building a knowledge base for inducers with a SCD. This was be done by analyzing how certain flow characteristics, such as incidence angle and head rise, change once a SCD is introduced. Additionally, work was made to develop methods for predicting major pump performance metrics (such as head rise, incidence, and efficiency) for inducers that use a SCD, based on pump design.

There are several modes of cavitation instability that affect the performance of modern inducers including rotating cavitation, alternate-blade cavitation, cavitation surge, and vortex cavitation. The research compared the cavitation effects of identical three and four-bladed inducers. CFD simulations were run at design flow coefficient and at 60% flow coeffecient with varying inlet pressures in order to analyze the effects of cavitation for both inducer configurations as they go through breakdown.

At design flow rates, there were very small differences between the three and four-blade inducers. Both inducers behaved very stably, except for a minimal appearance of rotating cavitation at a cavitation number of about $\sigma = 0.044$ for both inducers. The largest difference for the on-design cases was the large increase in rotor forces that was nearly three times larger for the three-bladed inducer than for the four-blade.

At off-design flow rates, the differences between the two inducers became much more apparent. Overall, the four-blade had a higher head rise than the three-blade ($\psi_{norm} = 1.42$ compared to $\psi_{norm} = 1.33$). The largest difference, however, was in the forces experienced by the rotor.

For higher cavitation numbers (greater than $\sigma \approx 0.058$), the four-blade had no noticeable instability present, whereas the three-blade had noticeable rotating cavitation for cavitation numbers as high as $\sigma \approx 0.139$. It is most likely due to a combination of the existence of rotating cavitation at these higher cavitation numbers and its asymmetric nature that the three-blade experienced forces that were much higher than those of the four-blade (with normalized maximum forces around 100 for the three-blade compared to around 10 for the four-blade).

For lower cavitation numbers ($\sigma < 0.037$), both the four and three-blade inducers experience a surging vapor cavity upstream of the inducer. The four-blade's upstream cavity was symmetrically balanced in the duct and grew much larger than for the three-blade case. In addition to being smaller than the four-blade's cavity, the three-blade's cavity formed to one side of the duct and rotated with the rotor. It may be because of the larger oscillations with the growth and collapse of the four-blade's cavity that rotor forces for the four-blade increased to match those for the three-blade cases.

Because of the reduced rotor forces, the symmetric formation of cavitation surge and alternate-blade cavitation, and the delayed inception of cavitation instabilities at 60% flow coefficient, the four-bladed inducer configuration was chosen to be used in future phases of this research.

This thesis has begun the work of analyzing non-cavitating flow characteristics for inducers with varying blade angles with a SCD attached. The presence of the SCD introduces recirculating flow that creates a locally increased mass flow rate through a portion of the inducer. It was shown in this research that the increased mass flow generated by the SCD helped to significantly reduce blade tip incidence when operating at off-design flow coefficients, compared to identical inducers without a SCD. At the lowest flow coefficient of $\phi = 0.014$, The I7no (no SCD) had a tip incidence angle of 31.9° compared to the I7 incidence of -1.6°. Further research showed that specifically for the I7no (no SCD) at a flow coefficient of $\phi = 0.028$, reverse flow was observed starting at about 87% blade span. In contrast, no reverse flow was observed for the I7 at any point along the blade. In fact, the recirculating flow through the SCD increased the axial velocity starting at a blade span of about 70%. The increased axial velocity for blade span greater than 70% caused the incidence angle to decrease in that region. This may imply that the inducer's blade profile needs

to be adjusted in order to accommodate the increased velocity caused by the recirculating flow and prevent the negative incidences from occurring.

It was shown that it is possible to predict the level of mass flow gain from the inlet blade tip angle for inducers with varying inlet blade angles. With the equations presented in this research, it was possible to predict the mass flow gain with a mean average percent error of 2.8%. Mass flow gain was shown to increase with increasing blade angles and decreasing flow coefficient.

It was also shown that there exists correlations between efficiency and head rise with mass flow gain. With the equations presented in this research, it was possible to predict head rise and efficiency for the inducers used in this study with a mean average percent error of 5.0% and 4.4% respectively. Head coefficient increases with mass flow gain, but levels out at a flow coefficient of about 3.7. This may imply that designing an inducer with a mass flow gain greater than 3.7 doesn't have any advantage in regards to head rise. Efficiency displayed a negative relationship with increasing mass flow gain. It was also shown that the accuracy of these equations require that the inducers share at least the same solidity. Future work will need to further investigate how other distinguishing physical characteristics (such as SCD passage and blade shape) can affect these relationships.

6.2 Recommendations

Through this research, it was shown that the accuracy of the equations derived in chapter 5 require that the inducers share at least the same solidity. It's possible that there exist other parameters upon which those equations depend that were inadvertently kept constant. It is recommended that future work further investigate how other distinguishing physical characteristics (such as SCD passage and blade shape) may affect the relationships established in chapter 5. Additionally, work should be done to incorporate those distinguishing physical characteristics, such as solidity, into a more robust method for predicting performance than the current method in chapter 5.

It was also shown that incorporating a SCD can drastically alter the flow characteristics throughout the inducer. Such changes should be considered on future inducer design. For example, understanding that axial velocity is greatly increased in the region closer to the shroud starting at a blade span of about 70%, it may be better to adjust the blade profile to ensure the ideal nominal

incidence angle of $+2^{\circ}$ [2]. Further research may investigate how such an adjustment affects cavitation behavior and the inducer's breakdown point.

REFERENCES

[1] Oliphant, K., 2013. "Inducer design for stable high suction performance, wide operating range, and increased structural robustness utilizing a high mass flow gain inlet cover treatment." *60th JANNAF Joint Propulsion Meeting, CPIA/JHU*. vii, viii, 3, 24, 43, 44, 45

[2] Brennen, C. E. *Hydrodynamics of Pumps*. Oxford University Press, Oxford, England. vii, 3, 9, 18, 24, 44, 45, 67

[3] Krise, J., 2011. "Characterization of high inlet diffusion low flow coefficient inducer pumps for space propulsion in the presence of a cavitation control device." Master of science, Brigham Young University, Provo, UT 84602, April. vii, viii, 3, 4, 10, 46, 47, 64

[4] Jakobsen, J., 1971. *Liquid Rocket Engine Turbopump Inducers*. NASA SP-8052, p. 12. vii, 6, 7, 24, 25, 44

[5] Japikse, D., 2001. "Overview of industrial and rocket turbopump inducer design." *CAV 2001: Fourth International Symposium on Cavitation*. 2, 3, 6

[6] Lobanoff, V. S., and Ross, R. R., 1992. *Centrifugal Pumps Design and Application*. Gulf Publishing Company, Houston, TX. 2

[7] Brennen, C., 2011. An introduction to cavitation fundamentals WIMRC Forum, University of Warwick, July. 7

[8] Tsujimoto, Y., Horiguchi, H., and Yonexawa, K., 2010. "Cavitation instabilities in turbopump inducers." *International Journal of Fluid Machinery and Systems,* **3**(2). 8, 18, 25, 26

[9] Tsujimoto, Y., 2001. "Simple rules for cavitation instabilities in turbomachinery." In *CAV2001: Fourth International Symposium on Cavitation*, California Institute of Technology. 8, 26, 44

[10] Agostino, L., and Salvetti, M., 2007. *Fluid Dynamics of Cavitation and Cavitating Turbopumps*. International Centre for Mechanical Sciences (CISM). 8

[11] Acosta, A. J., Tsujimoto, Y., Yoshida, Y., Azuma, S., and Cooper, P., 2001. "Effects of leading edge sweep on the cavitating characteristics of inducer pumps." *International Journal of Rotating Machinery*. 9

[12] Chang, N., Ganesh, H., Yakushiji, R., and Ceccio, S. L., 2011. "Tip vortex cavitation suppression by active mass injection." *Journal of Fluids Engineering*. 9

[13] Platzer, G. P., and Souders, W. G., 1981. "Tip vortex cavitation characteristics and delay of inception on a three-dimensional hydrofoil." *DTNSRDC Technical Report No. 81/007*. 10

[14] Kang, D., Arimoto, Y., Yonezawa, K., Horiguchi, H., Kawata, Y., Hah, C., and Tsujimoto, Y., 2010. "Suppression of cavitation instabilities in an inducer by circumferential groove and explanation of higher frequency components." *International Journal of Fluid Machinery and Systems,* **3**(2). 26

[15] CD-adapco *STAR-CCM+ Version 7.04.006 User Guide*. Melville, NY USA. 28, 29, 51

[16] Otsuka, S., Tsujimoto, Y., Kamijyo, K., and Furuya, O., 1996. "Frequency dependence of mass flow gain factor and cavitation compliance of cavitating inducers." *Journal of Fluids Engineering,* **118**(3), pp. 400–408. 44

[17] Acosta, A., 1955. A note on partial cavitation of flat plate hydrofoils Calif. Inst. Of Tech. Hydro Lab. Report No. E-19.9. 44